International Journal of Solids and Structures 182–183 (2020) 236–253

Contents lists available at ScienceDirect

International Journal of Solids and Structures

journal homepage: www.elsevier.com/locate/ijsolstr

Geometry-dependent stretchability and stiffness of ribbon kirigami based on large curvature curved beam model

Yafei Wang[a,b], Changguo Wang[a,b,*], Huifeng Tan[a,b]

[a] National Key Laboratory of Science and Technology for National Defence on Advanced Composites in Special Environments, Harbin Institute of Technology, Harbin 150080, PR China

[b] Center for Composite Materials, Harbin Institute of Technology, Harbin 150001, PR China

ARTICLE INFO

Article history:
Received 27 July 2018
Revised 12 June 2019
Accepted 5 August 2019
Available online 14 August 2019

Keywords:
Ribbon kirigami
Stiffness
Stretchability
Curved beam
Optimization

ABSTRACT

This paper lays stress on the normalized stiffness and stretchability of planar ribbon kirigami. A dimensionless analytical model is proposed based on plane strain beam theory, in which the large curvature curved beam (LCCB) model is considered. The tensile experiments and simulations are performed and compared to validate the analytical model based on four dimensionless parameters. It is found that not all kirigami-based design is conducive to the enhancement of normalized stretchability. Remarkable long arm effect can enhance the normalized stretchability or reduce the normalized stiffness by several orders of magnitude. Finally, an optimization method is used to obtain the maximum normalized stretchability. The results in this paper can be used to guide the kirigami design in future application.

1. Introduction

Kirigami, as a unique art form, primarily points to excise the paper at specific locations. Recently, kirigami has gained considerable anticipation among scientists as a superior design paradigm in various engineering fields. In particular, krigami-engineered elasticity (Callens and Zadpoor, 2017) is proposed as an ideal approach towards stretchable electronics (Guan et al., 2018; Shyu et al., 2015), diffraction gratings (Xu et al., 2016), force sensors (Blees et al., 2015), solar trackers (Lamoureux et al., 2015), soft deployable reflectors (Wang et al., 2017), sun-shading (Tang et al., 2017), and triboelectric generators (Wu et al., 2016).

Meanwhile, several design strategies have been developed to research the krigami-engineered elasticity. For the first design strategy, the thin sheets can be regularly excised using the pattern of straight cut, which the mechanism involving the post-buckling (Rafsanjani and Bertoldi, 2017) of kirigami motifs can guarantee the krigami-engineered elasticity. Especially, Blees et al. (2015) opened a new era towards one-atom-thick material kirigami. Isobe and Okumura (2016) carried out scaling law derivations and experiments to unveil the transition mode between in-plane and out-of-plane responses of kirigami. More recently, Yang et al. (2018) performed theory model construction using energy approach and a set of experimental and numerical studies on multistable kirigami. Upon uniaxial tensile loading, the thin kirigami structure can buckle out-of-plane as lateral bending consumes less energy than in-plane bending, allowing it undergoing ultimate tensile strain and achieving in situ tunable mechanical properties. The second strategy is combining the first strategy of straight cuts to create fractal design in 2D sheet, but the kirigami structure has a huge thickness to provide in-plane deformation of units around the hinges, which the lateral buckling is suppressed. Cho and coworkers demonstrated the substantial increasing of stretchability could be obtained by an enhanced level of hierarchy (Cho et al., 2014; Tang et al., 2015). The design principle with kirigami-based expandability of $>$ 800% greatly expands the design space for pluripotent materials, and leads to a manageable set of design paradigms (Shan et al., 2015; Tang and Yin, 2017) especially for stretchability modifications of brittle materials.

In addition to the abovementioned design strategies, variable geometrical design is crucial to create new opportunities for multipotent materials and structures (Dias et al., 2017; Holmes, 2019). The promising design strategy concerning geometry-dependent ribbon kirigami in this paper is inspired by the pattern of curve cut from Chinese paper art. Similar to the second design strategy involving the in-plane mechanical responses, the huge thickness of ribbon kirigami can suppress its lateral buckling under the uniaxial tension (Hwang and Bartlett, 2018; Jang et al., 2017; Xu et al., 2016). However, the research into mechanical performance of geometry-dependent planar ribbon krigami is scarce, and this

* Corresponding author at: Center for Composite Materials, Harbin Institute of Technology, Harbin 150001, PR China.
E-mail address: wangcg@hit.edu.cn (C. Wang).

https://doi.org/10.1016/j.ijsolstr.2019.08.007
0020-7683/

Nomenclature

R	The arc radius
α	The arc angle
ω	The ribbon width
$\bar{\omega}$	The ribbon width/radius ratio
l	The arm length
$\bar{l}$	The arm length/radius ratio
m	The connection length
$\bar{m}$	The connection length/radius ratio
L	The length of the unit cell
L_1	Two outer arc crest length between two hinge joints
$\bar{L}_1$	The dimensionless form of L_1
L_2	The half distance between two adjacent unit cells
$\bar{L}_2$	The dimensionless form of L_2
L_3	The distance of in-plane breadth
$\bar{L}_3$	The dimensionless form of L_3
$\bar{k}_{eff}$	The normalized stiffness
$\bar{\varepsilon}$	The normalized stretchability
M_0	The balancing moment
F	The end force
F'	The end force of a straight beam
u_{app}	The applied displacement
u'_{app}	The applied displacement of a straight beam
N	The internal normal force
V	The internal shear force
M	The internal moment
$\bar{N}$	Internal normal force for $F=1$
$\bar{V}$	Internal shear force for $F=1$
$\bar{M}$	Internal moment for $F=1$
U	The elastic deformation energy
A	The area of cross section
E	The plane strain modulus
$\bar{E}$	Young's modulus
G	Shear modulus
$\bar{\mu}$	The Poisson's ratio
I	The second-area moment of cross section
S	The static moment of the cross section on neutral axis
κ	The correction coefficient of strain energy
ε^f_{app}	The elastic stretchability
ε^f_{mat}	The intrinsic failure strain
ε_{app}	The applied strain
ε_{max}	The maximum tensile strain
σ_{arc}	The hoop stress in curve beam
θ	The angular variable
s_1	The arc-length variable
s_2	The linear variable
t	The scaling factor for in-plane breadth
r	The curvature radius of the neutral axis

is especially true for the cases of stiffness and stretchability. And the geometry effects including or excluding geometry constraints on the key mechanical responses of ribbon kirigami structures are rarely investigated as well.

Here, we report the geometry-dependent normalized stiffness and stretchability of ribbon kirigami with large thickness. The lateral buckling is suppressed. The plane strain beam and large curvature curved beam (LCCB) model are considered. Timoshenko and Goodier (1970) compared the elasticity theory with the LCCB theory and beam theory in the case of pure bending of the beam with different width/radius ratio (rectangular cross-section). They found that LCCB solution was in good agreement with elasticity solution. The relative error of pure bending normal stress between beam theory and LCCB solution was always smaller than 7% for width/radius ratio $<$ 0.2. While, due to their large margin of relative error when width/radius ratio $\geq$ 0.2, it was unsuitable to evaluate the large curvature curved beam using beam theory. Therefore, to design, evaluate and develop ribbon-kirigami-based stretchable devices, it is necessary and significant to provide a theoretical framework based on the appropriate analytical model.

This paper is organized as follows. Section 2 establishes analytical model of normalized stiffness and normalized stretchability using Castigliano's theorem and Moore Integral method. The corresponding derivations based on elasticity theory and beam theory are provided. The numerical and experimental methods are summarized in Section 3. Section 4 is dedicated to the comparison of analytical solution with experiments and simulations. Section 5 presents the designing of maximum normalized stretchability under geometry constraints. Finally, Section 6 gives the concluding remarks.

2. Analytical model

The kirigami structure we explored in this research is established by considering one-directional periodic boundary condition. For the sake of depicting our design paradigm, a typical kirigami unit cell is illustrated in Fig. 1a. The first key parameter to characterize the kirigami structure is arm length (l). The connection length (m) is then designated to adjust the distances between two adjacent unit cells. In this model, we consider a curved section (arc) between two arms, which the arcs can be described by the radius (R) and arc angle (α). Thus, the length L of a kirigami unit cell can be calculated by $L=2(R\cos\alpha - l\sin\alpha + m)$. And the kirigami structure can become a straight ribbon if $\alpha = -\pi/2$.

Through dimensional analysis method, four independent dimensionless parameters can vigorously define the proposed kirigami structure, the width of ribbon/radius $\bar{\omega}=\omega/R$, the length of connection/radius $\bar{m}=m/R$, the length of arm/radius $\bar{l}=l/R$ and arc angle α. Thereby, design variables possess four degrees of freedom in the design space of kirigami structures as illustrated in Fig. 1c, adapted from Yang et al. (2016). A series of kirigami structures can be described by different combinations of these four parameters, which the representative geometries are systematically summarized in Fig. 1c.

A uniaxial force (F) in the periodicity direction is applied at the end of connection. And it is customary to use the symmetry as the simplified measures in material mechanics. As seen in Fig. 1b, the connection section is firstly separated out and the remaining one quarter of the kirigami structure can be designated as a simplified analytical model. Then this process is performed by clamping its left end, the right end is considered free and subjected to a balancing force $F/2$ and a balancing moment M_0.

As the current research intends to provide insights into geometry-dependent mechanical responses involving large width/radius ratio. Closed-form analytical results for the key mechanics of kirigami structures are derived by considering the plane strain beam theory and large curvature curved beam (LCCB) model, as detailed in Appendix A.

In particular, normalized stiffness is the first important mechanical behavior, and it can be defined according to Eq. (1):

$$\bar{k}_{eff} = \frac{F}{F'} \cdot \frac{u'_{app}}{u_{app}} \tag{1}$$

where u_{app} is the applied displacement for F in the connection section, F' and u'_{app} are end force and applied displacement of a straight beam when $\alpha=-\pi/2$, respectively. The second key mechanics index is normalized stretchability, it is determined using a

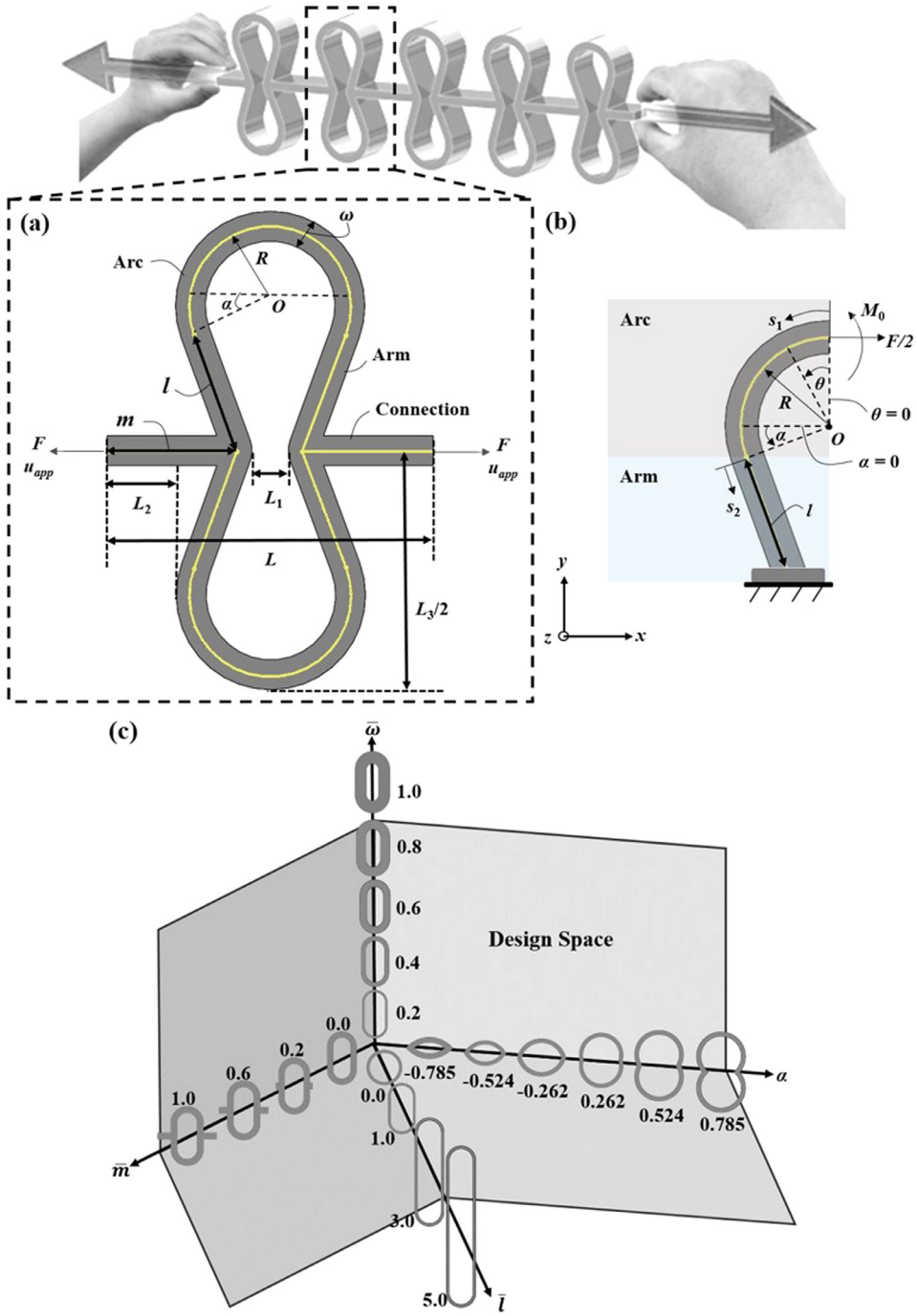

Fig. 1. (a) Illustration of a typical kirigami unit cell with geometry parameters and boundary conditions labeled. (b) Schematic of simplified analytical model for a kirigami unit cell and direction of internal forces labeled. (c) Design space for ribbon kirigami defined by four independent dimensionless parameters ($\bar{\omega}$, $\bar{l}$, $\bar{m}$ and α). (For interpretation of the references to color in text, the reader is referred to the web version of this article.)

continued equality:

$$\bar{\varepsilon} = \frac{\varepsilon_{app}^{f}}{\varepsilon_{mat}^{f}} = \frac{\varepsilon_{app}}{\varepsilon_{max}} \tag{2}$$

where ε_{app}^{f} and ε_{mat}^{f} are respectively the elastic stretchability and intrinsic failure strain of material, ε_{app} and ε_{max} represent the applied strain and the maximum tensile strain of kirigami structure, separately. The failure criterion we used here is $\varepsilon_{max} = \varepsilon_{mat}^{f}$. For brittle materials, ε_{mat}^{f} signifies corresponding rupture strain.

As the simplified analytical model in Fig. 1b is a statically indeterminate problem, the unknown M_0 should be determined first. In Appendix A, utilizing the Castigliano's theorem gives the following equation for solving M_0:

$$M_0 = \frac{F\left[\left(-2AlR + Al^2S + 2lS\right)\cos\alpha + AR(I\pi + 2lS + 2I\alpha + 2lS\sin\alpha)\right]}{2A[2lS + I(\pi + 2\alpha)]} \tag{3}$$

It is noteworthy that the advantage of using kirigami structure with large thickness/width ratios is that the lateral buckling can be suppressed. The effective approach adopted in the current research uses unit thickness models based on the two-dimensional plane strain. Expression of the relevant parameters from Eq. (3) can be

given in terms of unit thickness, i.e.

$$A=\omega,\quad I=\frac{\omega^3}{12},\quad S=\omega\left(R-\frac{\omega}{\ln\frac{2R+\omega}{2R-\omega}}\right) \tag{4}$$

where A is the area of cross section, I is the second-area moment of cross section, S is the static moment of the cross section on neutral axis. With the function of M_0 in hand, the Moore Integral method is then adopted in Appendix A to determine the normalized stiffness and stretchability of kirigami structure. Based on Eq. (1), the normalized stiffness containing the geometry parameters ($\bar{\omega}$, $\bar{l}$, $\bar{m}$ and α) is given using the following relationship:

$$\bar{k}_{eff}=\frac{80J\bar{\omega}^2\left(24J\bar{l}+(\pi+2\alpha)\bar{\omega}^2\right)Z_1}{\left[\begin{array}{l}480J^2\bar{l}^4+480J\bar{l}^2\bar{\omega}^2+1872J^2\bar{l}^2\bar{\omega}^2+1920J^2\bar{l}\bar{m}\bar{\omega}^2+480J\bar{l}\pi\bar{\omega}^2+696J^2\bar{l}\pi\bar{\omega}^2\\+80J\bar{l}^3\pi\bar{\omega}^2+960J\bar{l}\alpha\bar{\omega}^2+1392J^2\bar{l}\alpha\bar{\omega}^2+160J\bar{l}^3\alpha\bar{\omega}^2-40\bar{\omega}^4+80J\bar{\omega}^4-40J^2\bar{\omega}^4\\+98J\bar{l}\pi\bar{\omega}^4+80J\bar{m}\pi\bar{\omega}^4+10\pi^2\bar{\omega}^4+29J\pi^2\bar{\omega}^4+196J\bar{l}\alpha\bar{\omega}^4+160J\bar{m}\alpha\bar{\omega}^4+40\pi\alpha\bar{\omega}^4\\+116J\pi\alpha\bar{\omega}^4+40\alpha^2\bar{\omega}^4+116J\alpha^2\bar{\omega}^4+2\cos 2\alpha Z_2+\bar{\omega}^2\sin 2\alpha Z_3\end{array}\right]} \tag{5}$$

The normalized stretchability based on Eq. (2) can be related to geometry parameters ($\bar{\omega}$, $\bar{l}$, $\bar{m}$ and α) by

$$\bar{\varepsilon}=\frac{\left[\begin{array}{l}480J^2\bar{l}^4+480J\bar{l}^2\bar{\omega}^2+1872J^2\bar{l}^2\bar{\omega}^2+1920J^2\bar{l}\bar{m}\bar{\omega}^2+480J\bar{l}\pi\bar{\omega}^2+696J^2\bar{l}\pi\bar{\omega}^2\\+80J\bar{l}^3\pi\bar{\omega}^2+960J\bar{l}\alpha\bar{\omega}^2+1392J^2\bar{l}\alpha\bar{\omega}^2+160J\bar{l}^3\alpha\bar{\omega}^2-40\bar{\omega}^4+80J\bar{\omega}^4-40J^2\bar{\omega}^4\\+98J\bar{l}\pi\bar{\omega}^4+80J\bar{m}\pi\bar{\omega}^4+10\pi^2\bar{\omega}^4+29J\pi^2\bar{\omega}^4+196J\bar{l}\alpha\bar{\omega}^4+160J\bar{m}\alpha\bar{\omega}^4+40\pi\alpha\bar{\omega}^4\\+116J\pi\alpha\bar{\omega}^4+40\alpha^2\bar{\omega}^4+116J\alpha^2\bar{\omega}^4+2\cos 2\alpha Z_2+\bar{\omega}^2\sin 2\alpha Z_3\end{array}\right]}{\frac{40\bar{\omega}^2Z_1}{2-\bar{\omega}}\left[(1-J)\bar{\omega}\left(24J\bar{l}+(\pi+2\alpha)\bar{\omega}^2\right)-Z_4\cos\alpha-Z_5\sin\alpha\right]} \tag{6}$$

where Z_1, Z_2, Z_3, Z_4, Z_5 and J are provided in Appendix A (see Eq. (A18) and Eq. (A27)).

To provide a more useful form of analytical result to an experimentalist in designing kirigami-based devices, the special case for $\alpha=0$ is given as follows, and the normalized stretchability can be approximately calculated as

$$\bar{\varepsilon}(\alpha=0)\approx\frac{\left(-24+3\pi^2+2\bar{m}\pi\bar{\omega}^2+4\bar{l}\bar{m}\bar{\omega}^2+6\bar{l}\pi+24\bar{l}^2+4\bar{l}^3\pi+2\bar{l}^4\right)}{6\bar{\omega}(\bar{m}+1)\left(\pi-2+2\bar{l}+\bar{l}^2\right)} \tag{7}$$

So far, key mechanics indexes towards normalized stiffness and stretchability have been provided. Preliminary inspection of Eq. (5) is performed, and we find that the relations between normalized stiffness and $\bar{\omega}$, $\bar{m}$, $\bar{l}$are monotonic, separately. However, it is difficult to determine the effect of α on normalized stiffness. Because of complexity, we cannot facilely find the relation between normalized stretchability and four independent dimensionless parameters in Eq. (6). And thus, further analysis should be suitably carried out, as we provided in Section 4.

Additionally, to provide a full understanding of the LCCB model on stretchability of kirigami structures, the analytical model is compared with the series-expansion-term-dependent elasticity solution derived in Appendix B and degenerated LCCB solution (beam theory) derived in Appendix C. According to the linear elasticity and small deformation assumption, this process is also performed in Section 4.

3. Simulation and experiment methods

Finite Element Method (FEM): Simulation analysis is performed with the use of plane strain FEM in the ABAQUS code. Our material properties are similar to ones used in other studies of the stretchability of silicon (Lu and Yang, 2015). Young's modulus is $\bar{E}=130$ GPa, Poisson ratio is $\bar{\mu}=0.27$. The size of elements is carefully determined by using convergence test. Thus, all FEM models have the same size level of 0.1ω. Nominal strain of 0.02 is externally applied to the whole models and the corresponding coupling point should be correctly selected.

Experiment: Each kirigami structure is manufactured using 3D-printed Somos® Imagine 8000 resin material. The tensile experiment using INSTRON 5965, US is conducted to validate the analytical model. Concretely speaking, the specimen is slowly and carefully clamped with antiskid, and then the strain is measured as precisely as possible with the high-precision non-contacting video extensometer (the measurement accuracy (axial and transverse) is $\pm 2.5\,\mu$m). A strain ratio of 0.001 s^{-1} is used which produced the exact stress-strain curve. According to Eq. (2), one has to separately check the strain in a curved beam and in a straight beam. The elastic stretchability is determined by using a number of kirigami structures, while the corresponding straight specimen ($\alpha=-\pi/2$) is carefully measured for intrinsic failure strain, in order to get exact results of normalized stretchability. Finally, the stress-stain curve, elastic stretchability and intrinsic failure strain of kirigami structures with different geometries can be experimentally obtained to determine their normalized stretchability. If the obtained experimental data are found in accordance with the theory and FEM results, our LCCB theory modeling can provide insights into the rational design and practice of planar ribbon kirigami.

4. Results and discussion

4.1. Effects of geometry parameters on the normalized stiffness

Figs. 2 and 3 provide the comparison of analytical solutions and FEM results for plane strain model we proposed. Fig. 2a–f reveal the geometry-dependent normalized stiffness using the reciprocal of Eq. (5). As the normalized stiffness mentioned here involves the contributions of curved beam and straight beam ($\alpha=-\pi/2$). Therefore, if we designate the same applied displacement or end force, the Eq. (5) can be simplified as F/F' or u'_{app}/u_{app}, based on which considerable FEM computations can be avoided. As illustrated from Fig. 2a to f, analytical solution according to Eq. (5) is plotted as the solid lines, and FEM results are described by the filled rectangles. Design space for kirigami structure defined by four independent dimensionless parameters and representative geometries are displayed in the insets. The first design variable (independent variable) is represented by axis that marked with red color, while the second design variable is represented by green coordinate axis (Yellow marked coordinate axis represents the third design variable see Fig. 2g and h). Blue marked coordinate axis signifies invariant that the variable is fixed in the design space. Over the whole domain, the FEM results are in excellent agreement with the analytical solutions, which can be attributed to the appropriate derivation involving the consideration of LCCB, application of Castigliano's theorem, and execution of Moore Integral method. We

firstly investigate the effect of α on normalized stiffness, which is the burning question as mentioned above. Obviously, Fig. 2e and f show that with increasing of the first design variable α the normalized stiffness is monotonic increasing. However, two important observations should be reported: first, when α is closed to $-\pi/2$, it causes a drastic drop of $1/\bar{k}_{eff}$. In particular, if the kirigami structure devolves into a straight beam, a direct consequence of $1/\bar{k}_{eff} = 1$ can be obtained according to Eq. (1). Second, the reciprocal of normalized stiffness $1/\bar{k}_{eff}$ is increasing due to α increasing, till somewhere from 0 to 1, the solid line converges to the corresponding asymptotic line, indicating that the kirigami structures are geometry-constrained and non-overlapped. Geometrically, if $\bar{\omega}$, $\bar{m}$ and $\bar{l}$ have been fixed in kirigami structures, the penetration of internal material, because of the variation of arc angle α, is not allowed. To give a further explanation of geometry constraint, we will systematically discuss it in Section 5.

Comparing Fig. 2a to f, while the effect patterns of $\bar{\omega}$, $\bar{m}$, α and $\bar{l}$ on normalized stiffness, as outlined in Section 2, are all monotonic, for instance, the smaller $\bar{l}$, the larger $\bar{\omega}$, the smaller α, and the larger $\bar{m}$ will generate larger $\bar{k}_{eff}$. Reduction of normalized stiffness can be attained more than several orders of magnitude by simple kirigami design instead of straight ribbon. For example, in the case of $\bar{\omega} = 0.2$, $\bar{l} = 3$ and $\bar{m} = 0$ (see Fig. 2f), the normalized stiffness of kirigami structure is decreased by 366.53 times as compared with that of the straight beam when α is increasing from $-7\pi/18$ to $\pi/12$. These constitute dramatic evidences of the ultra-low stiffness for kirigami ribbons in terms of graphene kirigami (Qi et al., 2014), MoS_2 kirigami (Hanakata et al., 2016) and paper kirigami (Hua et al., 2017) in the stage of initial rigid response (Isobe and Okumura, 2016). Depending on the number of invariants, the reciprocal of normalized stiffness $1/\bar{k}_{eff}$ in relation to two invariants has been investigated as indicated in Fig. 2a–f. By appropriately designating the design variables, Fig. 2g and h provide insights into the normalized stiffness $\bar{k}_{eff}$ of kirigami structure with respect to one invariant. The color bar represents the value of $\bar{k}_{eff}$ according to the combination from the first to third design variable. The blank space represents the overlapping geometry for kirigami structure. The red dots as listed in Fig. 2g and h represent the partial geometries with different design variables, which are also prepared in the FEM simulations. The most comprehensive understanding stemmed from Fig. 2g and h is that 3D graphs give us not only the identical results to graphs in Fig. 2a to

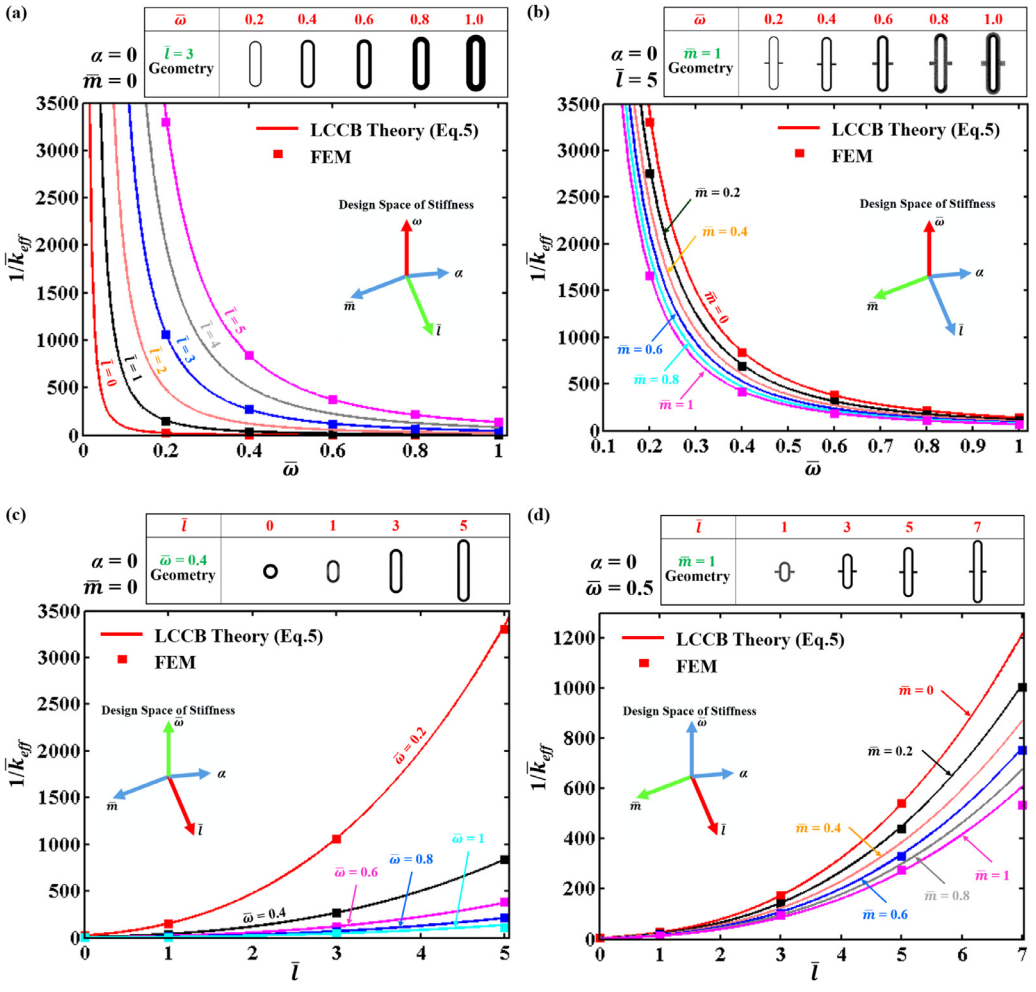

Fig. 2. (a) The reciprocal of normalized stiffness versus the first design variable $\bar{\omega}$ when the second design variable is $\bar{l}$ and invariants are $\alpha = 0$, $\bar{m} = 0$. (b) The reciprocal of normalized stiffness versus the first design variable $\bar{\omega}$ when the second design variable is $\bar{m}$ and invariants are $\alpha = 0$, $\bar{l} = 5$. (c) The reciprocal of normalized stiffness as a function of the first design variable $\bar{l}$ when the second design variable is $\bar{\omega}$ and invariants are $\alpha = 0$, $\bar{m} = 0$. (d) The reciprocal of normalized stiffness as a function of the first design variable $\bar{l}$ when the second design variable is $\bar{m}$ and invariants are $\alpha = 0$, $\bar{\omega} = 0.5$. (e) The reciprocal of normalized stiffness versus the first design variable α when the second design variable is $\bar{l}$ and invariants are $\bar{m} = 0$, $\bar{\omega} = 0.2$. (f) The reciprocal of normalized stiffness versus the first design variable α when the second design variable is $\bar{m}$ and invariants are $\bar{l} = 3$, $\bar{\omega} = 0.2$. Representative geometries are displayed in the insets. (g) Distribution of the normalized stiffness for the first design variable $\bar{l}$, the second design variable $\bar{m}$, the third design variable $\bar{\omega}$ and invariant $\alpha = 0$. (h) Distribution of the normalized stiffness for the first design variable α, the second design variable $\bar{m}$, the third design variable $\bar{l}$ and invariant $\bar{\omega} = 0$. (For interpretation of the references to color in text, the reader is referred to the web version of this article.)

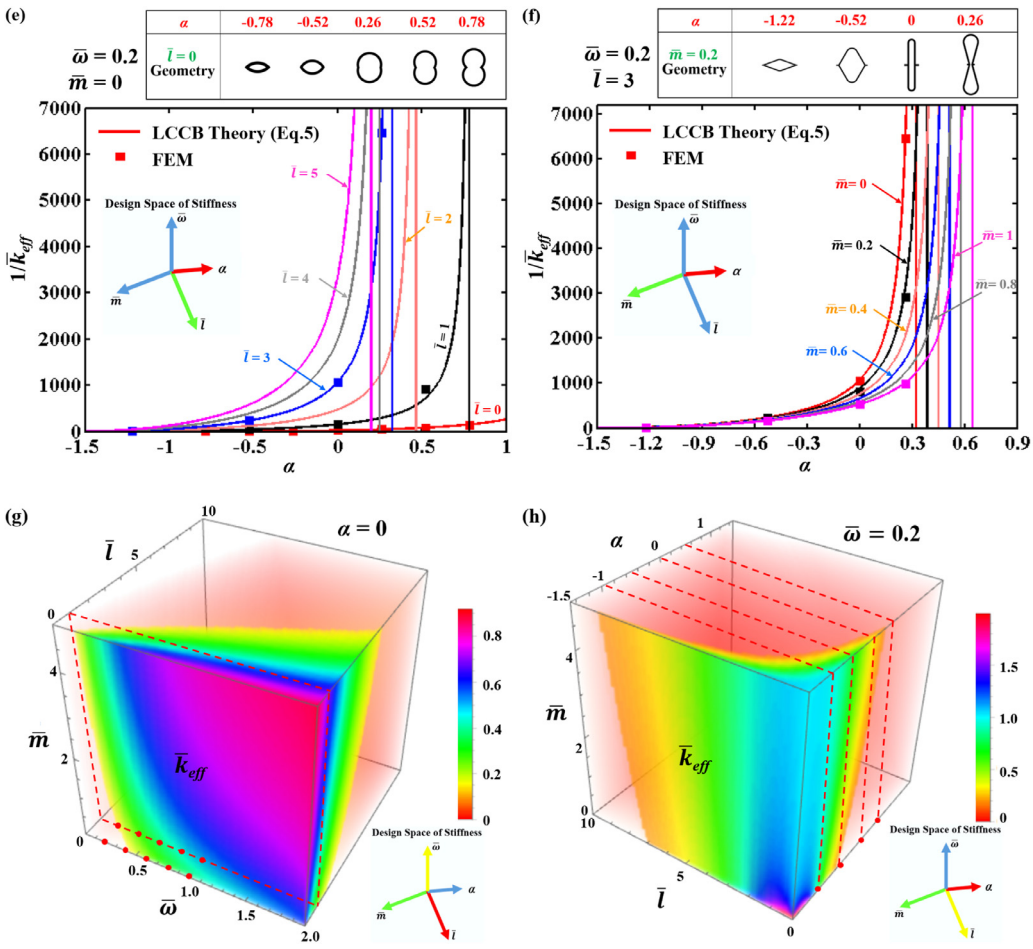

Fig. 2. Continued

f but also the broader landscapes and scopes of four independent dimensionless parameters.

4.2. Effects of geometry parameters on the normalized stretchability

Fig. 3 reveals the effects of geometric parameters on normalized stretchability by using the reciprocal of Eq. (6). Generally speaking, the FEM results show excellent agreement with the analytical solution according to Eq. (6), which the analytical and FEM solutions are separately plotted as the solid lines and filled rectangles. Fig. 3a and b provide typical evolutions for the increasing of $\bar{\omega}$: the effect of the first design variables are monotonic. But the corresponding second design variables are obviously different, which are respectively related to the arm length/radius $\bar{l}$ and length/radius $\bar{m}$. With increasing of $\bar{\omega}$ the normalized stretchability $\bar{\varepsilon}$ decreases, indicating that the large $\bar{\omega}$, in principle, is always adverse to the in-plane rigid rotation of kirigami structures. In other words, the pure bending strain accounts for a large proportion as compared with that of the small ribbon width/radius ratio $\bar{\omega}$. However, for the potential applications, such as kirigami structures for integrated solar tracking (Lamoureux et al., 2015), the minimum width/radius ratio $\bar{\omega}$ will restrict the device performance (such as GaAs kirigami tracker). Therefore, there is an urgent need to design a very stretchable kirigami structure under certain geometric constraints. Toward this end, by considering the non-overlapping conditions, the most stretchable ribbon kirigami with a specific in-plane breadth is designed in Section 5. It is apparent that $\bar{\varepsilon}$ will increase if $\bar{l}$ increases as indicated in Fig. 3a or $\bar{m}$ decreases in Fig. 3b for given $\bar{\omega}$. And for all cases listed in Fig. 3a and b, stretchability enhancement of kirigami structure due to $\bar{l}$ is significant. For example, in the case of $\alpha = 0$, $\bar{\omega} = 0.4$ and $\bar{m} = 0$, the normalized stretchability $\bar{\varepsilon}$ is increased by a factor of 18 when $\bar{l}$ increases from 0 to 5, which signifies the attractive ability for kirigami design presents a desirable technology in reducing the intrinsic tensile strain. Fig. 3c and d give a further investigation of the arm length/radius $\bar{l}$, which the second design variables are ribbon width/radius $\bar{\omega}$ and connection length/radius $\bar{m}$, respectively. As $\bar{l}$ increases, a sharp drop of the reciprocal of normalized stretchability $1/\bar{\varepsilon}$ can be observed as evident in Fig. 3c and d. Therefore, this gives rise to so-called long arm effect of kirigami structure. The contribution of long arm effect on stretchability enhancement of ribbon kirigami is in accordance with previous experiment and simulation results, such as those for kirigami nanocomposites as diffraction gratings reported by Xu et al. (2016), for kirigami-based force sensors reported by Blees et al. (2015), for stretchable kirigami polymer with high electrical conductivity reported by Guan et al. (2018), and for conducting kirigami composites as stretchable electrodes reported by Shyu et al. (2015). The effect of the first design variable α on $1/\bar{\varepsilon}$ is visible in Fig. 3e and f, and the second design variables are separately designated as $\bar{l}$ and $\bar{m}$. In comparison with the monotonicity of α in Figs. 2 and 3, we find that the curves in Fig. 3e are not all monotonic. For small arm length/radius such as $\bar{l} = 0$, Fig. 3e display the evolution for the α increasing from -1.5: first a linear increase of $1/\bar{\varepsilon}$ followed by a drop, after which the reciprocal of normalized stretchability $1/\bar{\varepsilon}$ varies in a lesser extent. But the curves become monotonic (due to the long arm effect) when $\bar{l}$ is large, which in-plane enhanced rigid rotation due to large $\bar{l}$ suppress the in-plane bending effect. Strik-

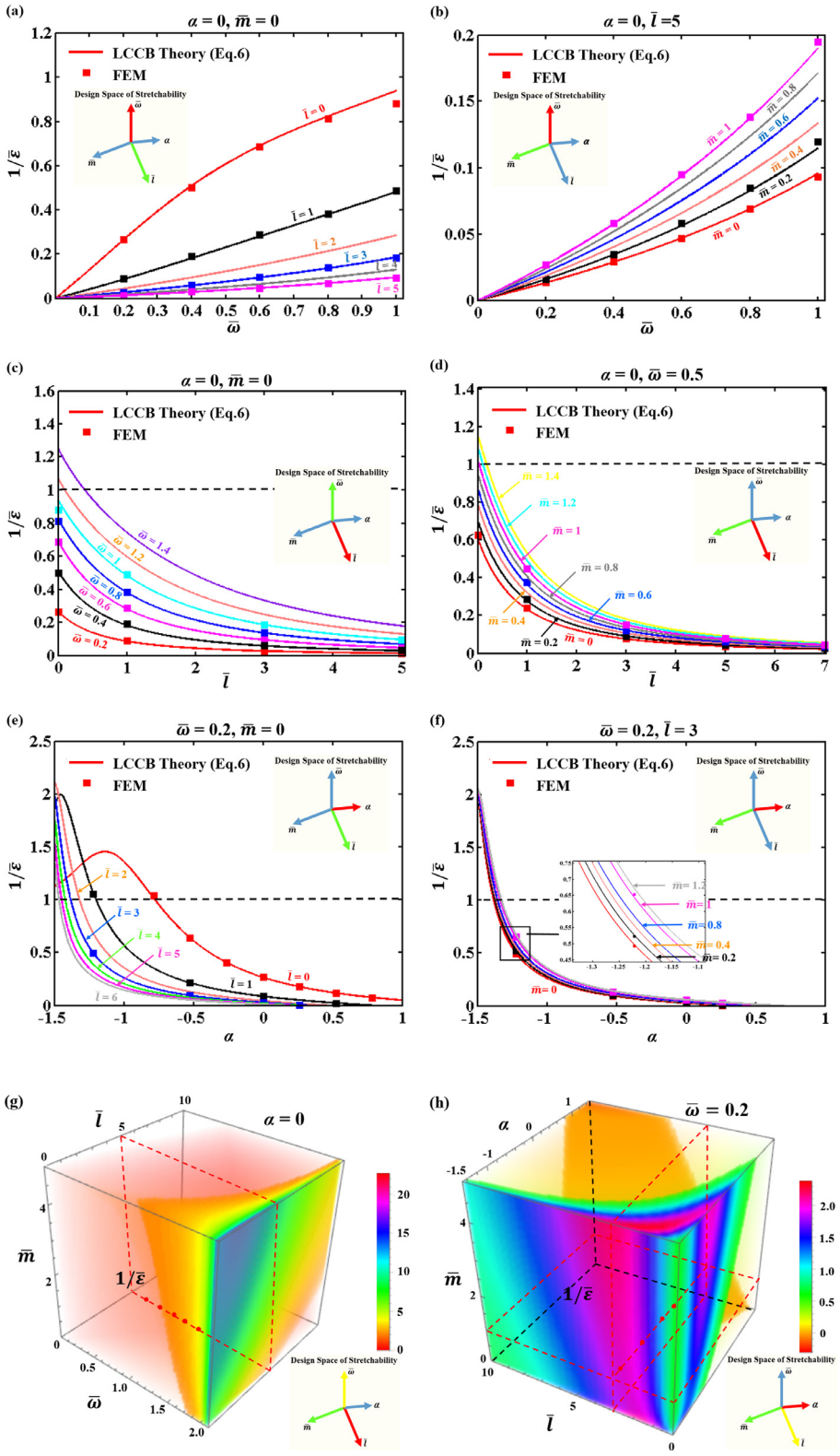

Fig. 3. (a) The reciprocal of normalized stretchability versus the first design variable $\bar{\omega}$ when the second design variable is $\bar{l}$ and invariants are $\alpha = 0$, $\bar{m} = 0$. (b) The reciprocal of normalized stretchability versus the first design variable $\bar{\omega}$ when the second design variable is $\bar{m}$ and invariants are $\alpha = 0$, $\bar{l} = 5$. (c) The reciprocal of normalized stretchability as a function of the first design variable $\bar{l}$ when the second design variable is $\bar{\omega}$ and invariants are $\alpha = 0$, $\bar{m} = 0$. (d) The reciprocal of normalized stretchability as a function of the first design variable $\bar{l}$ when the second design variable is $\bar{m}$ and invariants are $\alpha = 0$, $\bar{\omega} = 0.5$. (e) The reciprocal of normalized stretchability versus the first design variable α when the second design variable is $\bar{l}$ and invariants are $\bar{m} = 0$, $\bar{\omega} = 0.2$. (f) The reciprocal of normalized stretchability versus the first design variable α when the second design variable is $\bar{m}$ and invariants are $\bar{l} = 3$, $\bar{\omega} = 0.2$. (g) Distribution of the reciprocal of normalized stretchability for the first design variable $\bar{l}$, the second design variable $\bar{m}$, the third design variable $\bar{\omega}$ and invariant $\alpha = 0$. (h) Distribution of the reciprocal of normalized stretchability for the first design variable α, the second design variable $\bar{m}$, the third design variable $\bar{l}$ and invariant $\bar{\omega} = 0.2$. (For interpretation of the references to color in text, the reader is referred to the web version of this article.)

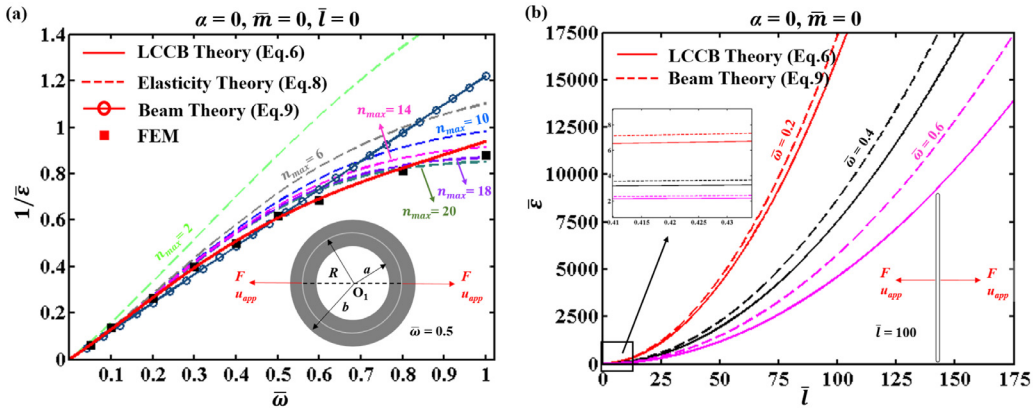

Fig. 4. (a) The reciprocal of normalized stretchability obtained from elasticity theory, LCCB theory, beam theory and FEM for specific ribbon kirigami with invariant $\alpha = 0$, $\bar{m} = 0$, $\bar{l} = 0$ as a function of $\bar{\omega}$. (b) The normalized stretchability obtained by LCCB theory solution and beam theory solution as a function of $\bar{l}$, and due to the long arm effect the normalized stretchability can be enhanced by several orders of magnitude. (For interpretation of the references to color in text, the reader is referred to the web version of this article.)

ingly, in some cases the reciprocal of normalized stretchability will exceed 1, this suggests that the maximum tensile strain ε_{max} may exceed the applied strain ε_{app} according to Fig. 3e, f and Eq. (2). Similar phenomena are also observed in Fig. 3c and d. These observations directly demonstrate that ribbon kirigami design by experience should be carefully carried out, and not all kirigami motifs are helpful to enhance the stretchability.

Fig. 3g and h reveal the effect of one invariant on the reciprocal of normalized stretchability $1/\bar{\varepsilon}$ according to Eq. (6), which this process is in line with the investigation of normalized stiffness in Fig. 2g and h. Red dots represent the cases where simulations are available. But the value of the color bar represents the magnitude of $1/\bar{\varepsilon}$ instead of $\bar{\varepsilon}$, and we have to plot it in such a form because of more friendly landscapes. The blank space, as reported above, represents the inaccessible geometries for ribbon kirigami, which can be obviously illustrated in Fig. 3g. Note that the arm length of ribbon kirigami can take a large value range when $\alpha = 0$. To give a full understanding of the long arm effect, we compare and investigate some extreme cases based on elasticity theory, LCCB theory and beam theory in Fig. 4. It is seen from Fig. 3h that the effect of α is nonmonotonic according to the color distribution, but it can bring substantial increases in the landscape of $1/\bar{\varepsilon}$. There is, in fact, much evidence to indicate that the previous design of kirigami structure by rule of thumb is not always able to provide a reliable guideline in enhancing the stretchability. Thus, the arc angle α should be precisely controlled in kirigami design. Moreover, for small α, large $\bar{l}$ is still a great motivator to decrease the reciprocal of normalized stretchability $1/\bar{\varepsilon}$ based on in-plane rigid rotation. Specifically, the significant reduction can be found in Fig. 3h where is represented by the counterintuitive yellow zone.

4.3. Comparison of different theoretical solutions

A combination of two dimensional plane strain elasticity theory, LCCB theory and beam theory is employed to analyze the normalized stiffness and stretchability. Based on boundary value condition and Airy's stress function in a series form, we use Fourier series expansion technology to obtain the elasticity solution. Here, the elasticity solution of normalized stretchability with specific geometry, as derived in Appendix B, is given, as follows:

$$(\bar{\varepsilon})_{Elasticity} = \frac{2\frac{A_0}{F}(1-\mu)\frac{b}{R} - \frac{B_0}{FbR}(1+\mu) - \sum_{n=2}^{\infty}\begin{bmatrix}(1+\mu)nb^{n-1}\frac{A_n}{RF} + (-2+n+2\mu+n\mu)b^{n+1}\frac{B_n}{RF} \\ -(1+\mu)nb^{-1-n}\frac{C_n}{RF} - (2+n-2\mu+n\mu)b^{-n+1}\frac{D_n}{RF}\end{bmatrix}}{2\frac{A_0}{F} - \frac{B_0}{Fa^2} + \sum_{n=2}^{\infty}\begin{pmatrix}(-1+n)na^{-2+n}\frac{A_n}{F} + (1+n)(2+n)a^n\frac{B_n}{F} \\ +(1+n)na^{-2-n}\frac{C_n}{F} + (1-n)(2-n)a^{-n}\frac{D_n}{F}\end{pmatrix}\cos\frac{n\pi}{2}} \tag{8}$$

where A_0/F, B_0/F, A_n/F, B_n/F, C_n/F and D_n/F are provided in Appendix B (see Eq. (B12)). LCCB solution of normalized stretchability can be calculated using Eq. (6), based on which the degenerated LCCB solution, that is, beam theory solution can be derived in Appendix C, and can be given by

$$(\bar{\varepsilon})_{Beam} = \frac{\begin{pmatrix}-12+12\bar{l}^2+\bar{l}^4+12\bar{l}\pi+2\bar{l}^3\pi+3\pi^2+24\bar{l}\alpha+4\bar{l}^3\alpha+12\pi\alpha+12\alpha^2 \\ +4\bar{l}\bar{m}\tilde{\omega}^2+\left(-12+12\bar{l}^2+\bar{l}^4-6\bar{l}(\pi+2\alpha)+2\bar{l}^3(\pi+2\alpha)\right)\cos 2\alpha \\ +3\left(6\bar{l}-\pi-2\alpha+2\bar{l}^2(\pi+2\alpha)\right)\sin 2\alpha+2\bar{m}\pi\tilde{\omega}^2+4\bar{m}\alpha\tilde{\omega}^2\end{pmatrix}}{6\tilde{\omega}\left(\bar{m}+\cos\alpha-\bar{l}\sin\alpha\right)\left(2\bar{l}+\pi+2\alpha+\left(-2+\bar{l}^2\right)\cos\alpha+2\bar{l}\sin\alpha\right)} \tag{9}$$

Fig. 4 contains the comparison of three theory solutions for normalized stretchability of specific kirigami structures according to Eqs. (6), (8) and (9). Generally speaking, results of LCCB theory solution (and FEM) show good agreement with the elasticity theory solution with high order series expansion in Fig. 4a, such as $n_{max} = 20$ according to Eq. (8), and both of them can accurately offer analytical solutions for a large range of ribbon width/radius $\tilde{\omega}$. But the results of beam theory are not perfectly as precise, which is expected as the over-simplification of pure bending effect is not suitable to describe the stretchability of LCCB. For all cases in Fig. 4a, two important facts should be given: firstly, elasticity solution is series-expansion-term-dependent. With increasing of n_{max} the relative error between elasticity theory solution and LCCB theory solution decreases. For example, elasticity solution curves can gradually converge to certain exact solution from $n_{max} = 2$ to $n_{max} = 20$. It will lead to an excessively large computations when we designate $n_{max} > 21$, while the obtained results have a negligible error. Secondly, due to the nature of beam theory it is not thought to provide a reliable estimate of stretchability of kirigami structure with LCCB. According to Eq. (A22) in Appendix A, y/r can be omitted only when $y << r$ (i.e. slender beam) and the denominator of Eq. (A22) can degenerate into the second-area moment of cross section I. However, for the cases studied in the current paper regarding LCCB, y and r are comparable, thus it is difficult to predict the exact results of kirigami structures using beam theory. For example, in the case of ribbon width/radius $\tilde{\omega} = 0.8$ as we can see from Fig. 4a, the relative error between elasticity theory solution and beam theory solution would be as much

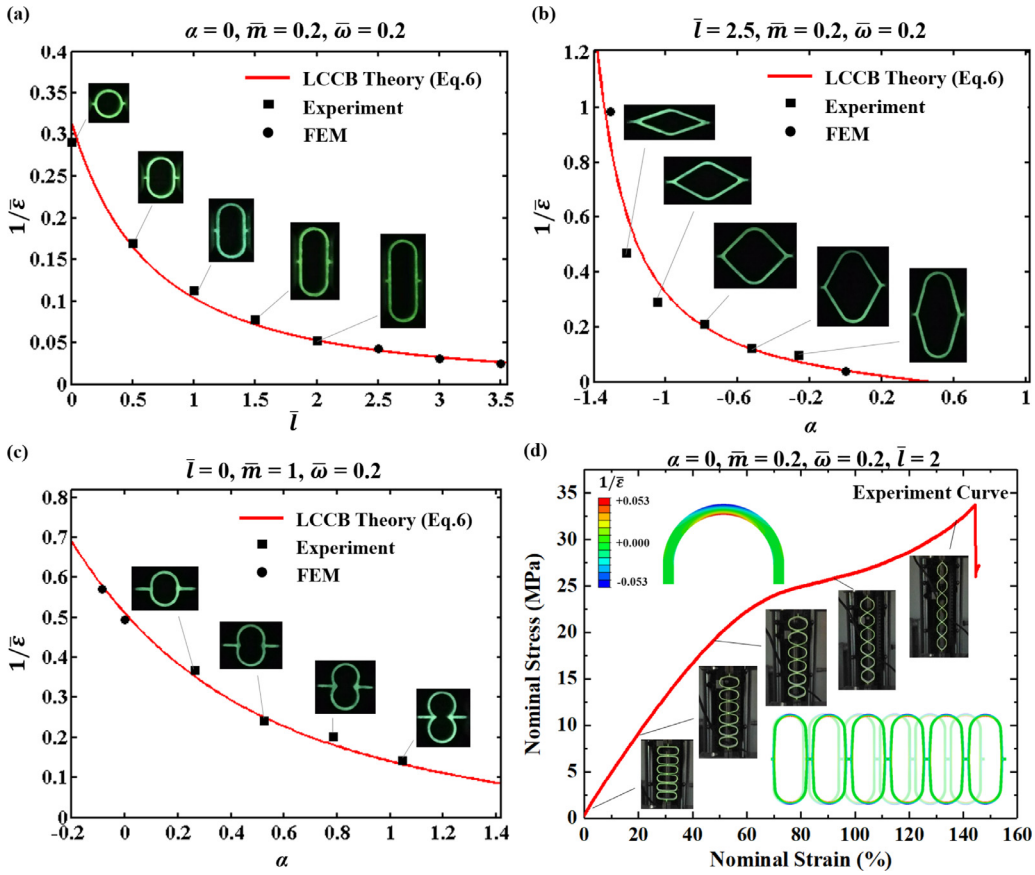

Fig. 5. (a) Comparison of experimental data and analytical modeling based on LCCB theory for the first design variable $\bar{l}$ and invariants $\alpha = 0$, $\bar{m} = 0.2$ and $\bar{\omega} = 0.2$. (b) and (c) Comparison of experimental data and analytical modeling by considering LCCB model for the first design variable α when invariants are $\bar{l} = 2.5$, $\bar{m} = 0.2$, $\bar{\omega} = 0.2$ and $\bar{l} = 0$, $\bar{m} = 1$, $\bar{\omega} = 0.2$. (d) The stress-strain curve of specific 3D-printed ribbon kirigami with $\alpha = 0$, $\bar{m} = 0.2$, $\bar{\omega} = 0.2$ and $\bar{l} = 2$. (For interpretation of the references to color in text, the reader is referred to the web version of this article.)

as 20.32%, while the LCCB theory solution compares favorably with the elasticity theory solution. Also, this remarkable difference can be found in Fig. 4b, and we suggest that careful analytical modeling should be established to evaluate the key mechanical behaviors of ribbon kirigami with LCCB. While the comparison produces a reliable and precise assessment, continuing researches will investigate a suite of assumptive strain extreme points and series convergence tests. It can also be observed from the Fig. 4b that long arm effect is powerful to enhance the normalized stretchability of kirigami structure, which could be nearly four orders of magnitude more stretchability enhancement. In other words, long arm effect can substantiality reduce the maximum tensile strain of kirigami structure. This property could be exploited for applications, such as stretchability modifications of intrinsic brittle materials under harsh environments, which require a trade-off between physical characteristics and intrinsic material properties.

4.4. Experimental validation

Fig. 5a–c provide comparison of theoretical solutions obtained from Eq. (6) and experimental results corresponding to different geometries. For all 3D-printed kirigami structures in Fig. 5, the large thickness/width ratio is designed to provide in-plane deformation and suppress the lateral buckling. The width of ribbon is 1 mm and the thickness of ribbon kirigami is 10 mm. Based on the nature of design space, Fig. 5a plots the effect of the first design variable $\bar{l}$ on the reciprocal of normalized stretchability $1/\bar{\varepsilon}$, while the corresponding three invariants are $\alpha = 0$, $\bar{m} = 0.2$ and $\bar{\omega} = 0.2$, respectively. In particular, for the case of $\alpha = 0$, $\bar{m} = 0.2$, $\bar{\omega} = 0.2$ and $\bar{l} = 2$, Fig. 5d shows the experimental stress-strain curve and the optical images of structural shapes at different strain levels. The strain field distribution in Fig. 5d obviously shows that the maximum strain in ribbon kirigami occurs at the inner arc crest, which is always the break location of 3D printed ribbon kirigami under uniaxial tension. Fig. 5b and c present the results of $1/\bar{\varepsilon}$ from analytical solution, as a function of the first design variables α, and the invariants are separately designated as $\bar{l} = 2.5$, $\bar{m} = 0.2$, $\bar{\omega} = 0.2$ and $\bar{l} = 0$, $\bar{m} = 1$, $\bar{\omega} = 0.2$. Over the whole domain, we find the reciprocal of normalized stretchability for experimental specimens (black rectangle, Fig. 5a–c inset), is in surprisingly good agreement with our theoretical prediction, confirming that the analytical model in current research by considering LCCB model is highly effective to provide insights into the rational design and practice of planar ribbon kirigami. However, there is always room for improvement. Due to non-dimensionalization nature, expressions with regard to the key mechanics indexes should be scale-scalable. To trigger further investigation and validate the scalability of analytical modeling, molecular dynamics (MD) simulation experiments for low dimensional silicon kirigami are performed in Appendix D. It is seen from Fig. D1 that the results from MD simulation is essentially identical to the analytical solution, but much work should be devoted to accuracy enhancement of analytical modeling for low dimensional silicon kirigami. The authors hope to answer this question in the near future.

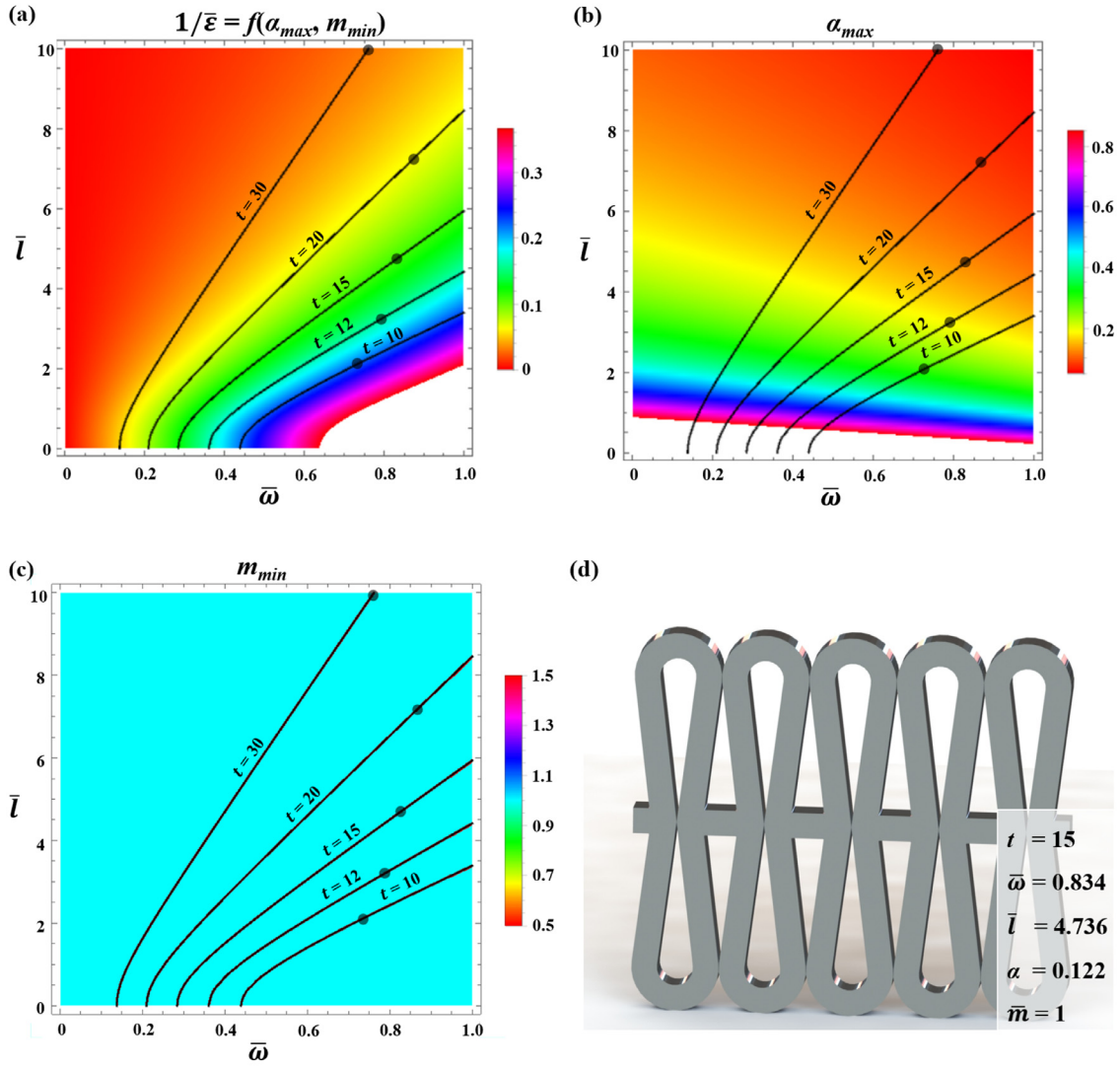

Fig. 6. (a) Distribution of the reciprocal of normalized stretchability for the first design variable $\bar{\omega}$ and $\bar{l}$, and the reciprocal of normalized stretchability is the function of α_{max} and $\bar{m}_{min}$. (b) and (c) Distribution of α_{max} and $\bar{m}_{min}$ for the first design variable $\bar{\omega}$ and $\bar{l}$, the optimization results can be calculated numerically based on the "number shape union" technology. (d) The optimal kirigami shape with the maximum normalized stretchability under geometry constraints when $t = 15$ and ($\bar{\omega}$, $\bar{l}$, α, $\bar{m}$) = (0.834, 4.736, 0.122, 1). (For interpretation of the references to color in text, the reader is referred to the web version of this article.)

5. Optimization

This paper has highlighted three facts associated with imperative optimization of kirigami structures under geometry constraint conditions: firstly, the analytical results of normalized stiffness and normalized stretchability indicate that geometry-constrained and non-overlapped conditions are intrinsic according to Eqs. (5) and (6). And not all kirigami shapes are acceptable within the scope of our present study. Secondly, the object of current research is modeled by considering one-directional periodic boundary condition. Thus the non-overlapped condition should be applied between the adjacent unit cells. Thirdly, while the larger $\bar{l}$ and the smaller $\bar{\omega}$ will generate larger normalized stretchability, sometimes it is impossible to achieve the maximum length or the minimum width of ribbon kirigami because of technical bottlenecks (such as resolution restriction of photolithography Widlund et al., 2014). Moreover, novel physical devices in relation to kirigami configurations, as mentioned above, also need geometry constraints to maintain their device performance. As a consequence of requirement for theory and application, based on the aforementioned three facts this section aims to achieve the maximum normalized stretchability under three geometry constraints.

By revisiting the geometry parameters in Fig. 1a and b, we find that three key parameters with regard to geometry constraints are not defined (L_1, L_2 and L_3). Here we start by describing the first geometry parameter: the distance of the outer arc crest between two hinge joints L_1. Obviously, the magnitude of L_1 is associated with the first non-overlapped condition. It is apparent that L_1 should be nonnegative. By applying the similar non-dimensionalization process, $\bar{L}_1$ can be expressed as L_1/R. Then, according to the nonnegativity condition, the definition of $\bar{L}_1$ can be given in terms of the three independent dimensionless parameters ($\bar{\omega}$, $\bar{l}$ and α), as follows:

$$\bar{L}_1 = 1 - \frac{\bar{\omega}}{2} - \left[\left(1 - \frac{\bar{\omega}}{2}\right)(1 - \cos\alpha) + \bar{l}\sin\alpha + \frac{\bar{\omega}}{2}(1 - \cos\alpha)\right] \geq 0 \tag{10}$$

L_2 represents the relationships between two adjacent unit cells, which is in relation to the second non-overlapped condition. If we define $\bar{L}_2$ as L_2/R, the dimensionless $\bar{L}_2$ can be related to four independent dimensionless parameters ($\bar{\omega}$, $\bar{l}$, $\bar{m}$ and α) by:

$$\bar{L}_2 = \bar{m} - \left[\bar{l}\sin\alpha + (1-\cos\alpha) + \frac{\bar{\omega}}{2}\right] \geq 0 \tag{11}$$

Based on Eqs. (10) and (11), the critical values of α and $\bar{m}$ with respect to geometry non-overlap can be determined using the following equations:

$$\alpha_{max} = 2\arctan\left(\frac{-2\bar{l} + \sqrt{4\bar{l}^2 + 4 - \bar{\omega}^2}}{2+\bar{\omega}}\right) \tag{12}$$

$$\bar{m}_{min} = \bar{l}\sin\alpha + (1-\cos\alpha) + \frac{\bar{\omega}}{2} \tag{13}$$

Then next step is to determine the third condition, that is, geometry constraint condition. According to the third fact, we need to designate a specific in-plane breadth to generate the kirigami motifs. Applying the normalization method, the dimensionless in-plane breadth $\bar{L}_3 = L_3/R$ can be expressed by

$$\bar{L}_3 = 2\left(1 + \frac{\bar{\omega}}{2} + \sin\alpha + \bar{l}\cos\alpha\right) = t\bar{\omega} \tag{14}$$

where t is the scaling factor. If we designate $t = 15$, it represents that the in-plane breadth of ribbon kirigami L_3 is 15 times larger than the ribbon width ω. Then combining the Eqs. (12), (13), (14) and (6), the optimization problem in regard to the maximum normalized stretchability under geometry constraints can be solved by using the "number shape union" technology. Concretely speaking, Eqs. (12) and (13) should be firstly substituted into Eq. (6), and we can obtain the normalized stretchability $\bar{\varepsilon}$ as the function of α_{max} and $\bar{m}_{min}$ by

$$\bar{\varepsilon} = g(\alpha_{max}, \bar{m}_{min}) \tag{15}$$

where the reciprocal of Eq. (15) is plotted in Fig. 6a. Both $\bar{\omega}$ and $\bar{l}$ are designated as the first design variables and defined in the design space of kirigami structures. Similarly, the color bar represents the value of $1/\bar{\varepsilon}$. Then with the aid of Eq. (14), ($\bar{\omega}$,$\bar{l}$) in the case of the minimum value $(1/\bar{\varepsilon})_{min}$ (i.e. $(\bar{\varepsilon})_{max}$) can be determined and represented by the black dots, as we can see in Fig. 6a. This process can be realized by utilizing the commercial software MATLAB or open-source software Anaconda (Python). With the obtained ($\bar{\omega}$, $\bar{l}$) in hand, we can shift the results represented by black dots into the functional drawing districts of Eq. (12) and Eq. (13), and the color bars in Fig. 6b and c separately represent the value of α_{max} and $\bar{m}_{min}$. Thus, the corresponding α and $\bar{m}$ can be determined according to Fig. 6b and Fig. 6c, respectively. By collecting the relevant parameters t and ($\bar{\omega}$, $\bar{l}$, α, $\bar{m}$), the maximum normalized stretchability under geometry constraints can be finally achieved. We investigate the cases when $t$is from 10 to 30 as shown in Fig. 6a–c. In the case of $t = 15$, the optimization results can be calculated numerically and given by ($\bar{\omega}$, $\bar{l}$, α, $\bar{m}$) = (0.834, 4.736, 0.122, 1), which the optimal shape of ribbon kirigami is illustrated in Fig. 6d. While the "number shape union" technology is not as perfect as the Lagrangian multiplier method, because of its simplicity, this can also accurately provide a result to guide the design of ribbon kirigami.

6. Conclusions

This paper has, through theoretical analysis and FEM, for the first time, systematically revealed geometry-dependent effect patterns of four dimensionless parameters on the normalized stiffness and stretchability of planar ribbon kirigami. Excellent accuracy and scalability of analytical solution by considering LCCB model are comprehensively verified by combining the tensile experiments, elasticity theories, beam theories, plane strain FEM and MD simulations. This study shows that the smaller normalized stiffness and the larger normalized stretchability, except for some counter-intuitive expectations, can be realized by the larger $\bar{l}$, the smaller $\bar{\omega}$, the smaller $\bar{m}$ and the larger α. Not all kirigami configurations are conducive to the enhancement of normalized stretchability while the corresponding normalized stiffness decreases. Remarkable long arm effect can, in some case, carry tremendous potential which, is surprising for enhanced normalized stretchability and reduced normalized stiffness by several orders of magnitude. Based on three facts associated with geometry constraints, the maximum normalized stretchability can be obtained based on the "number shape union" technology. In brief, this paper provides a foundational research to guide the kirigami design in future application.

Acknowledgment

This work was supported by National Natural Science Foundation of China, 11572099 and 11872160.

The author wishes to thank Mrs. Zaiying Zhang and Mr. Gongran Wang for their thoughtful kindness. The author wishes to thank Dr. Jiawei Zhang for his technical supports. The author would like to express his thanks to the anonymous reviewers whose constructive comment significantly improved the paper.

Appendix A

Normalized stiffness is calculated using the following relationship:

$$\bar{k}_{eff} = \frac{F}{F'} \cdot \frac{u'_{app}}{u_{app}} \tag{A1}$$

According to free-body diagram and coordinates in Fig. 1b, the internal forces in the curved beam can be calculated by

$$\begin{cases} M_{arc} = \frac{FR}{2}(1-\cos\theta) - M_0 \\ V_{arc} = \frac{F}{2}\sin\theta \\ N_{arc} = \frac{F}{2}\cos\theta \end{cases} \tag{A2}$$

$$\begin{cases} M_{arm} = \frac{F}{2}[R(1+\sin\alpha) + s\cos\alpha] - M_0 \\ V_{arm} = \frac{F}{2}\cos\alpha \\ N_{arm} = -\frac{F}{2}\sin\alpha \end{cases} \tag{A3}$$

$$N_{connection} = F \tag{A4}$$

where N, V and M are respectively the internal normal force at the centroid, the internal shear force, and the internal moment of the cross section. Then, Castigliano's theorem is designated to obtain generalized displacement, and determination of boundary condition for $\theta = 0$ is according to Fig. 1a:

$$\frac{\partial U}{\partial M_0} = \frac{\partial (U_{arc} + U_{arm})}{\partial M_0} = 0 \tag{A5}$$

where U is the elastic deformation energy. As to arc section

$$U_{arc} = \int_0^{\left(\frac{\pi}{2}+\alpha\right)R} \left(\frac{M_{arc}^2}{2ESR} + \frac{M_{arc}N_{arc}}{EAR} + \frac{N_{arc}^2}{2EA} + \kappa\frac{V_{arc}^2}{2GA} \right) ds_1 \tag{A6}$$

as to arm section

$$U_{arm} = \int_0^{l} \left(\frac{N_{arm}^2}{2EA} + \kappa\frac{V_{arm}^2}{2GA} + \frac{M_{arm}^2}{2EI} \right) ds_2 \tag{A7}$$

where G is shear modulus, κ is correction coefficient for strain energy. Then the generalized displacements of arm and arc with respect to Eq. (A5) can be calculated from Eqs. (A6) and (A7):

$$\frac{\partial U_{arc}}{\partial M_0} = \frac{1}{4AES}[2F(AR-S)\cos\alpha - A(\pi+2\alpha)(FR-2M_0)] \tag{A8}$$

$$\frac{\partial U_{arm}}{\partial M_0} = \frac{Il}{4E}[F(l\cos\alpha + 2R(1+\sin\alpha)) - 4M_0] \tag{A9}$$

Expression of the corresponding parameters from Eqs. (A6) to (A9) can be given in terms of unit thickness:

$$A = \omega, \quad E = \frac{\bar{E}}{1-\bar{\mu}^2}, \quad I = \frac{\omega^3}{12}, \quad S = \omega\left(R - \frac{\omega}{\ln\frac{2R+\omega}{2R-\omega}}\right) \tag{A10}$$

where A is the area of cross section, E is plane strain modulus, $\bar{E}$ is Young's modulus, $\bar{\mu}$ is Poisson's ratio, I is the second-area moment of cross section, S is the static moment of the cross section on neutral axis.

Then the insertion of Eqs. (A8) and (A9) into Eq. (A5) gives the following equation for solving M_0:

$$M_0 = \frac{F\left[\left(-2AIR + Al^2S + 2IS\right)\cos\alpha + AR(I\pi + 2lS + 2I\alpha + 2lS\sin\alpha)\right]}{2A[2lS + I(\pi+2\alpha)]} \tag{A11}$$

where A, I and S are given in Eq. (A10). To establish the equation of normalized stiffness, the load-displacement relation needs to be determined. Besides, one more step of re-writing the internal equation has to be performed. Here, the Moore Integral method is adopted to determine the applied displacement:

$$u_{app} = 2\delta_{arc} + 2\delta_{arm} + \frac{Fm}{EA} \tag{A12}$$

where

$$\delta_{arc} = \int_0^{(\alpha+\frac{\pi}{2})R} \left(\frac{M_{arc}\bar{M}_{arc}}{ESR} + \frac{N_{arc}\bar{M}_{arc}}{EAR} + \frac{M_{arc}\bar{N}_{arc}}{EAR} + \frac{N_{arc}\bar{N}_{arc}}{EA} + \kappa\frac{V_{arc}\bar{V}_{arc}}{GA} \right) ds_1 \tag{A13}$$

$$\delta_{arm} = \int_0^{l} \left(\frac{N_{arm}\bar{N}_{arm}}{EA} + \kappa\frac{V_{arm}\bar{V}_{arm}}{GA} + \frac{M_{arm}\bar{M}_{arm}}{EI} \right) ds_2 \tag{A14}$$

We note that the results of M_{arm} and M_{arc} are corresponding new forms by combining the Eqs. (A2), (A3) and (A11). $\bar{N}_{arm}$, $\bar{V}_{arm}$, $\bar{M}_{arm}$, $\bar{N}_{arc}$, $\bar{V}_{arc}$ and $\bar{M}_{arc}$ are internal forces of the curved beam when $F = 1$. In consideration of load-displacement relation in the case of $\alpha = -\pi/2$, for the straight beam, we get

$$\frac{u'_{app}}{F'} = \frac{L}{2EA} \tag{A15}$$

where L is the length of the unit cell, together with the revisiting of Fig. 1a, it can be determined as

$$L = 2(R\cos\alpha - l\sin\alpha + m) \tag{A16}$$

With the function of u_{app} in hand, the normalized stiffness can be then obtained from Eqs. (A12), (A15), (A16) and (A1):

$$\bar{k}_{eff} = \frac{80J\bar{\omega}^2\left(24J\bar{l} + (\pi+2\alpha)\bar{\omega}^2\right)Z_1}{\left[\begin{array}{l}480J^2\bar{l}^4 + 480J\bar{l}^2\bar{\omega}^2 + 1872J^2\bar{l}^2\bar{\omega}^2 + 1920J^2\bar{l}\bar{m}\bar{\omega}^2 + 480J\bar{l}\pi\bar{\omega}^2 + 696J^2\bar{l}\pi\bar{\omega}^2 \\ +80J\bar{l}^3\pi\bar{\omega}^2 + 960J\bar{l}\alpha\bar{\omega}^2 + 1392J^2\bar{l}\alpha\bar{\omega}^2 + 160J\bar{l}^3\alpha\bar{\omega}^2 - 40\bar{\omega}^4 + 80J\bar{\omega}^4 - 40J^2\bar{\omega}^4 \\ +98J\bar{l}\pi\bar{\omega}^4 + 80J\bar{m}\pi\bar{\omega}^4 + 10\pi^2\bar{\omega}^4 + 29J\pi^2\bar{\omega}^4 + 196J\bar{l}\alpha\bar{\omega}^4 + 160J\bar{m}\alpha\bar{\omega}^4 + 40\pi\alpha\bar{\omega}^4 \\ +116J\pi\alpha\bar{\omega}^4 + 40\alpha^2\bar{\omega}^4 + 116J\alpha^2\bar{\omega}^4 + 2\cos 2\alpha Z_2 + \bar{\omega}^2\sin 2\alpha Z_3\end{array}\right]} \tag{A17}$$

where

$$Z_1 = \left(\bar{m} + \cos\alpha - \bar{l}\sin\alpha\right) \tag{A18-a}$$

$$Z_2 = \left(\begin{array}{l}-20\bar{\omega}^4 + 40\bar{\omega}^2 + 4J^2\left(60\bar{l}^4 + 114\bar{l}^2\bar{\omega}^2 - 5\bar{\omega}^4\right) \\ +J\bar{\omega}^2\left(240\bar{l}^2 + 40\bar{l}^3(\pi+2\alpha) + \bar{l}(\pi+2\alpha)\left(29\bar{\omega}^2 - 120\right)\right)\end{array}\right) \tag{A18-b}$$

$$Z_3 = \left(216J^2\bar{l} - 10(\pi+2\alpha)\bar{\omega}^2 + J\left(720\bar{l} + 240\bar{l}^2(\pi+2\alpha) + 49(\pi+2\alpha)\bar{\omega}^2\right)\right) \tag{A18-c}$$

$$J = 1 - \frac{\bar{\omega}}{\ln\frac{2+\bar{\omega}}{2-\bar{\omega}}} \tag{A18-d}$$

Another key mechanics index is normalized stretchability, it is determined by:

$$\bar{\varepsilon} = \frac{\varepsilon_{app}^f}{\varepsilon_{mat}^f} = \frac{\varepsilon_{app}}{\varepsilon_{max}} \tag{A19}$$

For normalized stretchability in Eq. (A19), the applied strain is defined as

$$\varepsilon_{app} = \frac{u_{app}}{L/2} \tag{A20}$$

where u_{app} and L are given in Eqs. (A12) and (A16), separately. With the aid of Eq. (A19), aim of the next step is to obtain the equation of ε_{max}. For a given large curvature curved beam (LCCB), effects of pure bending and axial tension are the major contributors to the variation of hoop stress. It is helpful to understand the pure bending of LCCB. Based on the assumption that normal stress is equal to zero between the longitudinal fibers, the stress of cross section can be preliminarily written as

$$\sigma = E\frac{1}{1+\frac{r}{y}}\frac{\delta(d\theta)}{d\theta} \tag{A21}$$

By using the equilibrium equation$M = \int_A y\sigma\, dA = 0$, the stress can be expressed in terms of the moment (M) as

$$\sigma = \frac{My}{\left(1+\frac{y}{r}\right)\int_A \frac{y^2}{(1+\frac{y}{r})}dA} \tag{A22}$$

where r is the curvature radius of the neutral axis. Therefore, the hoop stress in LCCB can be calculated according to Eq. (21) as

$$\sigma_{arc} = \frac{M_{arc}y}{\left(1+\frac{y}{r}\right)\int_A \frac{y^2}{(1+\frac{y}{r})}dA} + \frac{N_{arc}}{A} \tag{A23}$$

where

$$r = R(1-J) \tag{A24}$$

As the maximum strain in kirigami structure always occurs at the inner arc crest, which is acceptable based on Widlund et al. (2014) and Zhang et al. (2013). Applying the physical equation, the maximum tensile strain can be given using the following relationship:

$$\varepsilon_{max} = \frac{1}{E}\left(\frac{-M_0\left(R - \frac{\omega}{2} - r\right)}{S\left(R - \frac{\omega}{2}\right)} + \frac{F}{2A}\right) \tag{A25}$$

Finally, combining Eqs. (A19), (A20) and (A25), the normalized stretchability can be given by:

$$\bar{\varepsilon} = \frac{\left[\begin{array}{l}480J^2\bar{l}^4 + 480J\bar{l}^2\bar{\omega}^2 + 1872J^2\bar{l}^2\bar{\omega}^2 + 1920J^2\bar{l}\bar{m}\bar{\omega}^2 + 480J\bar{l}\pi\bar{\omega}^2 + 696J^2\bar{l}\pi\bar{\omega}^2 \\ +80J\bar{l}^3\pi\bar{\omega}^2 + 960J\bar{l}\alpha\bar{\omega}^2 + 1392J^2\bar{l}\alpha\bar{\omega}^2 + 160J\bar{l}^3\alpha\bar{\omega}^2 - 40\bar{\omega}^4 + 80J\bar{\omega}^4 - 40J^2\bar{\omega}^4 \\ +98J\bar{l}\pi\bar{\omega}^4 + 80J\bar{m}\pi\bar{\omega}^4 + 10\pi^2\bar{\omega}^4 + 29J\pi^2\bar{\omega}^4 + 196J\bar{l}\alpha\bar{\omega}^4 + 160J\bar{m}\alpha\bar{\omega}^4 + 40\pi\alpha\bar{\omega}^4 \\ +116J\pi\alpha\bar{\omega}^4 + 40\alpha^2\bar{\omega}^4 + 116J\alpha^2\bar{\omega}^4 + 2\cos 2\alpha Z_2 + \bar{\omega}^2\sin 2\alpha Z_3\end{array}\right]}{\frac{40\bar{\omega}^2 Z_1}{2-\bar{\omega}}\left[(1-J)\bar{\omega}\left(24J\bar{l} + (\pi+2\alpha)\bar{\omega}^2\right) - Z_4\cos\alpha - Z_5\sin\alpha\right]} \tag{A26}$$

where Z_1, Z_2, Z_3 and J are given according to Eq. (A18), Z_4 and Z_5 are respectively given as follows:

$$Z_4 = 2(2J-\bar{\omega})\left(-\bar{\omega}^2 + J\left(6\bar{l}^2 + \bar{\omega}^2\right)\right) \tag{A27-a}$$

$$Z_5 = 24J\bar{l}(2J-\bar{\omega}) \tag{A27-b}$$

It is noteworthy that the Eqs. (5) and (6) are the same as Eqs. (A17) and (A26), respectively.

Appendix B

The elasticity solution we derived here for the specific geometry ($\bar{l}=0$, $\bar{m}=0$, $\alpha=0$) can be described as the problem of a stretching circular ribbon with two opposite and equal forces along the diameter, as shown in Fig. 4a. Polar coordinate system is designated to solve the stress and strain field. According to the principle of Airy stress function (Timoshenko and Goodier, 1970), stress function can be structured as follows:

$$\phi = \sum_{n=2}^{\infty} \left(A_n r^n + B_n r^{n+2} + C_n r^{-n} + D_n r^{-n+2}\right) \cos n\theta + A_0 r^2 + B_0 \ln r \tag{B1}$$

where A_n, B_n, C_n, D_n, A_0 and B_0 are undetermined constants. After verification, Eq. (B1) satisfies the single-valued condition of displacement and compatible equation $\nabla^4\phi = (\frac{\partial^2}{\partial r^2} + \frac{1}{r}\frac{\partial}{\partial r} + \frac{1}{r^2}\frac{\partial^2}{\partial \theta^2})^2 = 0$.

For polar coordinate system, the stress components can be calculated using the following relations:

$$\begin{cases} \sigma_r = \frac{1}{r}\frac{\partial \phi}{\partial r} + \frac{1}{r^2}\frac{\partial^2 \phi}{\partial \theta^2} \\ \sigma_\theta = \frac{\partial^2 \phi}{\partial r^2} \\ \tau_{r\theta} = \frac{1}{r^2}\frac{\partial \phi}{\partial \theta} - \frac{1}{r}\frac{\partial^2 \phi}{\partial r \partial \theta} \end{cases} \tag{B2}$$

By substituting Eq. (B1) into Eq. (B2), the stress field can be written in terms of the undetermined constants as

$$\begin{cases} \sigma_r = \frac{1}{r}\left(2rA_0 + \frac{B_0}{r} + \sum_{n=2}^{\infty} \cos n\theta \left(nr^{-1+n}A_n + (2+n)r^{1+n}B_n - nr^{-1-n}C_n + (2-n)r^{1-n}D_n\right)\right) \\ + \frac{1}{r^2}\sum_{n=2}^{\infty} -n^2 \cos n\theta \left(r^n A_n + r^{2+n}B_n + r^{-n}C_n + r^{2-n}D_n\right) \\ \sigma_\theta = 2A_0 - \frac{B_0}{r^2} + \sum_{n=2}^{\infty} \cos n\theta \left((-1+n)nr^{-2+n}A_n + (1+n)(2+n)r^n B_n + (1+n)nr^{-2-n}C_n \right. \\ \left. + (1-n)(2-n)r^{-n}D_n\right) \\ \tau_{r\theta} = \frac{1}{r^2}\sum_{n=2}^{\infty} -n \sin n\theta \left(r^n A_n + r^{2+n}B_n + r^{-n}C_n + r^{2-n}D_n\right) \\ -\frac{1}{r}\sum_{n=2}^{\infty} -n \sin n\theta \left(nr^{-1+n}A_n + (2+n)r^{1+n}B_n - nr^{-1-n}C_n + (2-n)r^{1-n}D_n\right) \end{cases} \tag{B3}$$

Now, we suppose that two opposite and equal forces are applied to the small range, and the corresponding angle is Θ. Therefore, the applied force can be expressed using piecewise function as

$$F(\theta) = \begin{cases} \frac{F}{2b\Theta} & -\Theta \le \theta \le \Theta,\ \pi - \Theta \le \theta \le \pi + \Theta \\ 0 & \Theta < \theta < \pi - \Theta,\ \pi + \Theta < \theta < 2\pi - \Theta \end{cases} \tag{B4}$$

Next, Fourier series expansion technology is used here to achieve the calculation of $F(\theta)$:

$$F(\theta) = \frac{a_0}{2} + \sum_{i=1}^{\infty} a_i \cos 2i\theta = \frac{a_0}{2} + \sum_{\substack{i=1 \\ n=2i}}^{\infty} a_i \cos n\theta \tag{B5}$$

where

$$a_0 = \frac{2}{\pi}\int_{-\frac{\pi}{2}}^{\frac{\pi}{2}} \frac{F}{2b\Theta} d\theta = \frac{2F}{\pi b} \tag{B6}$$

$$a_i = \frac{2}{\pi}\int_{-\frac{\pi}{2}}^{\frac{\pi}{2}} \frac{F}{2b\Theta} \cos n\theta d\theta = \frac{2F \sin n\Theta}{\pi bn\Theta} \tag{B7}$$

Thus, combining the Eqs. (B5), (B6) and (B7), we obtain

$$F(\theta) = \frac{F}{\pi b} + \frac{2F}{\pi b}\sum_{n=2}^{\infty} \frac{\sin n\Theta}{n\Theta} \cos n\theta \tag{B8}$$

Applying $\lim_{\Theta \to 0} \frac{\sin n\Theta}{n\Theta} = 1$, gives

$$\sum_{n=2}^{\infty} \cos n\theta = -\frac{1}{2} \quad (\theta \neq 0, \theta - \pi \neq 0) \tag{B9}$$

So far, the preparatory work has be finished, and the next step is to determine the unknown constants based on the following boundary conditions:

$$\begin{cases} r = a, \sigma_r = 0 \\ r = a, \tau_{r\theta} = 0 \\ r = b, \sigma_r = F(\theta) \\ r = b, \tau_{r\theta} = 0 \end{cases} \tag{B10}$$

Then the substitution of Eqs. (B3) and (B8) into Eq. (B10) gives the following relationships for solving the undetermined constants:

$$\begin{cases} 2A_0+\frac{B_0}{a^2}=0 \\ (-1+n)na^{-2+n}A_n+(1+n)(-2+n)a^nB_n+(1+n)na^{-2-n}C_n \\ +(-1+n)(2+n)a^{-n}D_n=0 \\ (-1+n)a^{-2+n}A_n+(1+n)a^nB_n-(1+n)a^{-2-n}C_n-(-1+n)a^{-n}D_n=0 \\ 2A_0+\frac{B_0}{b^2}=\frac{F}{\pi b} \\ (-1+n)nb^{-2+n}A_n+(1+n)(-2+n)b^nB_n+(1+n)nb^{-2-n}C_n \\ +(-1+n)(2+n)b^{-n}D_n=-\frac{2F}{\pi b} \\ (-1+n)b^{-2+n}A_n+(1+n)b^nB_n-(1+n)b^{-2-n}C_n-(-1+n)b^{-n}D_n=0 \end{cases} \tag{B11}$$

This yields

$$\begin{cases} A_0/F=\frac{b}{2\pi\left(-a^2+b^2\right)} \\ B_0/F=-\frac{a^2b}{\pi\left(-a^2+b^2\right)} \\ A_n/F=-\frac{a^2b^{1+n}\left(-a^{2n}b^2+b^{2+2n}-a^{2+2n}n+a^{2n}b^2n\right)}{(-1+n)\pi\xi} \\ B_n/F=\frac{b^{1+n}\left(-a^{2+2n}+a^2b^{2n}-a^{2+2n}n+a^{2n}b^2n\right)}{(1+n)\pi\xi} \\ C_n/F=\frac{a^{2+2n}b^{1+n}\left(a^{2n}b^2-b^{2+2n}+a^2b^{2n}n-b^{2+2n}n\right)}{(1+n)\pi\xi} \\ D_n/F=-\frac{a^{2n}b^{1+n}\left(a^{2+2n}-a^2b^{2n}+a^2b^{2n}n-b^{2+2n}n\right)}{(-1+n)\pi\xi} \end{cases} \tag{B12}$$

where

$$\xi=a^{2+4n}b^2-2a^{2+2n}b^{2+2n}+a^2b^{2+4n}-a^{4+2n}b^{2n}n^2+2a^{2+2n}b^{2+2n}n^2-a^{2n}b^{4+2n}n^2 \tag{B13}$$

Now, fully analytical solutions for the stress components from elasticity theory are achieved according to Eqs. (B3) and (B12), and the normalized stretchability will be derived after we obtain the strain-displacement relation. Here, with the aid of generalized Hooke's law, we have

$$\begin{cases} \frac{\partial u}{\partial r}=\varepsilon_r=\frac{1}{E}(\sigma_r-\mu\sigma_\theta) \\ \varepsilon_\theta=\frac{1}{E}(\sigma_\theta-\mu\sigma_r) \\ \frac{\partial v}{\partial\theta}=r\varepsilon_\theta-u \\ \gamma_{r\theta}=\frac{2(1+\mu)}{E}\tau_{r\theta}=\frac{1}{r}\frac{\partial u}{\partial\theta}+\frac{\partial v}{\partial r}-\frac{v}{r} \end{cases} \tag{B14}$$

Combining the Eqs. (B3), (B12) and (B14), the following equation will be provided to solve the strain field:

$$\begin{aligned} &\frac{1}{r}\frac{\partial u}{\partial\theta}+\frac{\partial v}{\partial r}-\frac{v}{r} \\ &=\frac{1}{E}\sum_{n=2}^{\infty}\begin{bmatrix}2n(n-1)(1+\mu)r^{n-2}A_n+2n(1+n)(1+\mu)r^nB_n \\ -2n(1+n)(1+\mu)r^{-2-n}C_n-2n(n-1)(1+\mu)r^{-n}D_n\end{bmatrix}\sin n\theta \\ &\quad+\frac{1}{r}\frac{\partial p(\theta)}{\partial\theta}+\frac{\partial p_1(r)}{\partial r}+\frac{1}{r}\int p(\theta)d\theta-\frac{1}{r}p_1(r) \end{aligned} \tag{B15}$$

and the strain components can be expressed as follows:

$$u=\frac{1}{E}\left(2A_0(1-\mu)r-\frac{B_0}{r}(1+\mu)-\sum_{n=2}^{\infty}\begin{bmatrix}(1+\mu)nr^{n-1}A_n \\ +(-2+n+2\mu+n\mu)r^{n+1}B_n \\ -(1+\mu)nr^{-1-n}C_n \\ -(2+n-2\mu+n\mu)r^{-n+1}D_n\end{bmatrix}\cos n\theta\right)+p(\theta) \tag{B16}$$

$$v=\frac{1}{E}\sum_{n=2}^{\infty}\begin{bmatrix}(1+\mu)nr^{n-1}A_n \\ +(4+n+n\mu)r^{n+1}B_n \\ +(1+\mu)nr^{-1-n}C_n \\ +(-4+n+n\mu)r^{-n+1}D_n\end{bmatrix}\sin n\theta-\int p(\theta)d\theta+p_1(r) \tag{B17}$$

where A_n, B_n, C_n, D_n are given in Eq. (B12). Then substituting the Eqs. (B16) and (B17) into Eq. (B15), gives

$$\frac{1}{r}\frac{\partial p(\theta)}{\partial\theta}+\frac{\partial p_1(r)}{\partial r}+\frac{1}{r}\int p(\theta)d\theta-\frac{1}{r}p_1(r)=0 \tag{B18}$$

where $p(\theta)$ and $p_1(r)$ are unknown functions. Next, we designate $p_1(r)=Mr$ and $p(\theta)=H\sin\theta+K\cos\theta$. By utilizing the boundary conditions $\theta=0$, $v=0$ and$\theta=\frac{\pi}{2}$, $v=0$, $\frac{\partial v}{\partial r}=0$, the strain components can be finally written as

$$\begin{cases} u=\frac{1}{E}\left(2A_0(1-\mu)r-\frac{B_0}{r}(1+\mu)-\sum_{n=2}^{\infty}\begin{bmatrix}(1+\mu)nr^{n-1}A_n \\ +(-2+n+2\mu+n\mu)r^{n+1}B_n \\ -(1+\mu)nr^{-1-n}C_n \\ -(2+n-2\mu+n\mu)r^{-n+1}D_n\end{bmatrix}\cos n\theta\right) \\ v=\frac{1}{E}\sum_{n=2}^{\infty}\begin{bmatrix}(1+\mu)nr^{n-1}A_n \\ +(4+n+n\mu)r^{n+1}B_n \\ +(1+\mu)nr^{-1-n}C_n \\ +(-4+n+n\mu)r^{-n+1}D_n\end{bmatrix}\sin n\theta \end{cases} \tag{B19}$$

With the aid of the assumption of strain extreme point based on Widlund et al. (2014) and Zhang et al. (2013), the applied strain ε_{app} and the maximum tensile strain ε_{max} can next calculated using the following relationships:

$$\varepsilon_{app} = \frac{\frac{1}{E}\left(2A_0(1-\mu)b - \frac{B_0}{b}(1+\mu) - \sum_{n=2}^{\infty}\begin{bmatrix}(1+\mu)nb^{n-1}A_n \\ +(-2+n+2\mu+n\mu)b^{n+1}B_n \\ -(1+\mu)nb^{-1-n}C_n \\ -(2+n-2\mu+n\mu)b^{-n+1}D_n\end{bmatrix}\right)}{R\cos\alpha - l\sin\alpha + m} \tag{B20}$$

$$\varepsilon_{max} = \frac{1}{E}\left(2A_0 - \frac{B_0}{a^2} + \sum_{n=2}^{\infty}\left(\begin{matrix}(-1+n)na^{-2+n}A_n + (1+n)(2+n)a^nB_n \\ +(1+n)na^{-2-n}C_n + (1-n)(2-n)a^{-n}D_n\end{matrix}\right)\cos\frac{n\pi}{2}\right) \tag{B21}$$

Substitution of ε_{app} and ε_{max} into Eq. (2), gives the following equation for solving the normalized stretchability with respect to elasticity theory

$$\bar{\varepsilon} = \frac{2\frac{A_0}{F}(1-\mu)\frac{b}{R} - \frac{B_0}{FbR}(1+\mu) - \sum_{n=2}^{\infty}\begin{bmatrix}(1+\mu)nb^{n-1}\frac{A_n}{RF} + (-2+n+2\mu+n\mu)b^{n+1}\frac{B_n}{RF} \\ -(1+\mu)nb^{-1-n}\frac{C_n}{RF} - (2+n-2\mu+n\mu)b^{-n+1}\frac{D_n}{RF}\end{bmatrix}}{2\frac{A_0}{F} - \frac{B_0}{Fa^2} + \sum_{n=2}^{\infty}\left(\begin{matrix}(-1+n)na^{-2+n}\frac{A_n}{F} + (1+n)(2+n)a^n\frac{B_n}{F} \\ +(1+n)na^{-2-n}\frac{C_n}{F} + (1-n)(2-n)a^{-n}\frac{D_n}{F}\end{matrix}\right)\cos\frac{n\pi}{2}} \tag{B22}$$

where $\mu = \bar{\mu}/(1-\bar{\mu})$, A_n/F, B_n/F, C_n/F, D_n/F, A_0/F and B_0/F are given in Eq. (B12). Lastly, we designate the value of $n_{\max}$ and corresponding normalized stretchability can be obtained by series expansion form. It is important to note that Eq. (B22) is the same as Eq. (8).

Appendix C

Based on LCCB theory derived in Appendix A, the framework of beam theory can be obtained, that is, if we designate $y/r << 1$, stress can be expressed as $\sigma = My/\int_A y^2 dA$. Thus, the denominator $\int_A y^2 dA$ has been degenerated into the second-area moment of cross section I.

For the sake of simplicity, we utilize the same methods to determine the normalized stretchability as compared with that of LCCB theory in the following derivation. Firstly, the unknown moment M_0 should be determined. According to the free-body diagram, the internal forces are obtained and given in Eqs. (A2), (A3) and (A4). Then, based on internal force equations, elastic deformation energy for arm section and arc section can be calculated by:

$$U_{arc} = \int_0^{(\alpha+\frac{\pi}{2})R}\left(\frac{N_{arm}^2}{2EA} + \kappa\frac{V_{arm}^2}{2GA} + \frac{M_{arm}^2}{2EI}\right)ds_1 \tag{C1}$$

$$U_{arm} = \int_0^{l}\left(\frac{N_{arm}^2}{2EA} + \kappa\frac{V_{arm}^2}{2GA} + \frac{M_{arm}^2}{2EI}\right)ds_2 \tag{C2}$$

where κ is correction coefficient of strain energy. According to the Castigliano's theorem and the boundary condition, the following equation can be used to solve M_0:

$$\frac{\partial(U_{arc}+U_{arm})}{\partial M_0} = 0 \tag{C3}$$

Substituting Eqs. (C1), (C2) into Eq. (C3), gives

$$M_0 = \frac{F\left(\left(l^2-2R^2\right)\cos\alpha + R(2l+\pi R+2R\alpha+2l\sin\alpha)\right)}{4l+2R(\pi+2\alpha)} \tag{C4}$$

Next, we re-write the internal equations based on Eq. (C4) as follows

$$\begin{cases} M_{arc} = \frac{FR}{2}(1-\cos\theta) \\ -\frac{F\left(\left(l^2-2R^2\right)\cos\alpha+R(2l+\pi R+2R\alpha+2l\sin\alpha)\right)}{4l+2R(\pi+2\alpha)} \\ V_{arc} = \frac{F}{2}\sin\theta \\ N_{arc} = \frac{F}{2}\cos\theta \end{cases} \tag{C5}$$

$$\begin{cases} M_{arm} = \frac{F}{2}[R(1+\sin\alpha)+s\cos\alpha] \\ -\frac{F\left(\left(l^2-2R^2\right)\cos\alpha+R(2l+\pi R+2R\alpha+2l\sin\alpha)\right)}{4l+2R(\pi+2\alpha)} \\ V_{arm} = \frac{F}{2}\cos\alpha \\ N_{arm} = -\frac{F}{2}\sin\alpha \end{cases} \tag{C6}$$

$$N_{connection} = F \tag{C7}$$

By using the Moore Integral method, the load-displacement relation can be obtained according to Eq. (C8):

$$\begin{aligned} u_{app} = {} & 2\left(\int_0^{l}\left(\frac{N_{arm}\bar{N}_{arm}}{EA} + \kappa\frac{V_{arm}\bar{V}_{arm}}{GA} + \frac{M_{arm}\bar{M}_{arm}}{EI}\right)ds_2\right) \\ & + 2\left(\int_0^{(\alpha+\frac{\pi}{2})R}\left(\frac{N_{arc}\bar{N}_{arc}}{EA} + \kappa\frac{V_{arc}\bar{V}_{arc}}{GA} + \frac{M_{arc}\bar{M}_{arc}}{EI}\right)ds_1\right) + \frac{Fm}{EA} \end{aligned} \tag{C8}$$

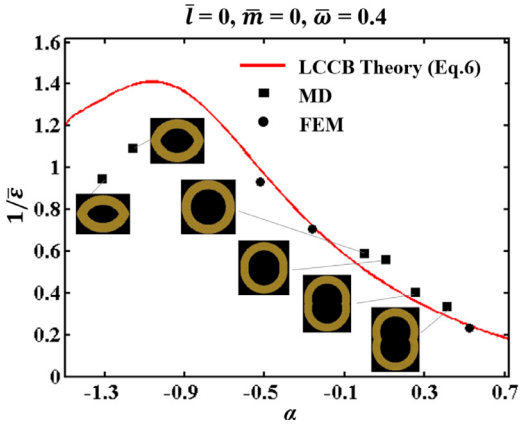

Fig. D1. Comparison of MD simulation results and analytical modeling for the first design variable α and invariants $\bar{l} = 0$, $\bar{m} = 0$ and $\bar{\omega} = 0.4$.

where $\bar{N}_{arm}$, $\bar{V}_{arm}$, $\bar{M}_{arm}$, $\bar{N}_{arc}$, $\bar{V}_{arc}$ and $\bar{M}_{arc}$ are corresponding internal forces when $F = 1$. Thereby, combining Eq. (C5)–Eq. (C8), the applied strain can be calculated. Moreover, the maximum strain can be given by

$$\varepsilon_{max} = \left(\frac{-M_0 y}{EI}\right)\Big|_{\theta=0}^{y=-\frac{\omega}{2}} \tag{C9}$$

Based on Eq. (2) or Eq. (A19), the normalized stretchability from beam theory in terms of four independent dimensionless parameters can be calculated using the following equation:

$$\bar{\varepsilon} = \frac{\begin{pmatrix} -12 + 12\bar{l}^2 + \bar{l}^4 + 12\bar{l}\pi + 2\bar{l}^3\pi + 3\pi^2 + 24\bar{l}\alpha + 4\bar{l}^3\alpha + 12\pi\alpha + 12\alpha^2 \\ +4\bar{l}\bar{m}\bar{\omega}^2 + \left(-12 + 12\bar{l}^2 + \bar{l}^4 - 6\bar{l}(\pi + 2\alpha) + 2\bar{l}^3(\pi + 2\alpha)\right)\cos 2\alpha \\ +3\left(6\bar{l} - \pi - 2\alpha + 2\bar{l}^2(\pi + 2\alpha)\right)\sin 2\alpha + 2\bar{m}\pi\bar{\omega}^2 + 4\bar{m}\alpha\bar{\omega}^2 \end{pmatrix}}{6\bar{\omega}\left(\bar{m} + \cos\alpha - \bar{l}\sin\alpha\right)\left(2\bar{l} + \pi + 2\alpha + \left(-2 + \bar{l}^2\right)\cos\alpha + 2\bar{l}\sin\alpha\right)} \tag{C10}$$

which the Eq. (9) is the same as Eq. (C10).

Appendix D

Because of non-dimensionalization nature, expression of the key mechanics is scalable. Corresponding to analysis of kirigami macrostructures via finite element methods, extensive atomistic simulations are performed to explore the kirigami nanostructures using MD engine LAMMPS (Plimpton, 1995). For low dimension silicon kirigami, the Erhart/Albe-Tersoff potential is applied to describe the Si-Si atoms interactions. Velocity-Verlet algorithm is applied to calculate the motion equation, and the time step is designated as 0.001 ps. Initial equilibrium of the system is relaxed at 0.1 K for 5 ps with the use of Nose-Hoover thermostat. After that, the displacement loadings (0.02 nm/ps) is applied on the right end of silicon kirigami, while the left end is fixed. For all cases in Fig. D1, the silicon kirigami structures with different geometries are generated by using in-house code, the nanoribbon width and thickness of silicon kirigami are 27.15 Å and 108.6 Å, respectively. Initial cracks should be introduced at the inner arc crest to control the propagation direction of nanocrack. Importantly, direction of the thickness should be designated as the periodic boundary condition, so that MD simulation of silicon kirigami can successfully simulate the plane strain model in this paper. Fig. D1 shows that the normalized stretchability of silicon kirigami is in line with the analytical solution based on LCCB theory, while we neglect the size effect of low dimension silicon kirigami. In future, we hope special care should be taken when nanoribbon kirigami plays a more important role in stretchable devices.

References

Blees, M.K., Barnard, A.W., Rose, P.A., Roberts, S.P., McGill, K.L., Huang, P.Y., Ruyack, A.R., Kevek, J.W., Kobrin, B., Muller, D.A., McEuen, P.L., 2015. Graphene kirigami. Nature 524, 204.

Callens, S.J.P., Zadpoor, A.A., 2017. From flat sheets to curved geometries: origami and kirigami approaches. Mater Today doi:10.1016/j.mattod.2017.10.004.

Cho, Y., Shin, J.H., Costa, A., Kim, T.A., Kunin, V., Li, J., Lee, S.Y., Yang, S., Han, H.N., Choi, I.S., Srolovitz, D.J., 2014. Engineering the shape and structure of materials by fractal cut. Proc. Natl. Acad. Sci. USA 111, 17390–17395.

Dias, M.A., McCarron, M.P., Rayneau-Kirkhope, D., Hanakata, P.Z., Campbell, D.K., Park, H.S., Holmes, D.P., 2017. Kirigami actuators. Soft Matter 13, 9087–9092.

Guan, Y.S., Zhang, Z., Tang, Y., Yin, J., Ren, S., 2018. Kirigami-Inspired nanoconfined polymer conducting nanosheets with 2000% stretchability. Adv. Mater. 30, e1706390.

Hanakata, P.Z., Qi, Z.A., Campbell, D.K., Park, H.S., 2016. Highly stretchable MoS2 kirigami. Nanoscale 8, 458–463.

Holmes, D.P., 2019. Elasticity and stability of shape-shifting structures. Curr. Opin. Colloid Interface Sci. 40, 118–137.

Hua, Z., Zhao, Y., Dong, S., Yu, P., Liu, Y., Wei, N., Zhao, J., 2017. Large stretchability and failure mechanism of graphene kirigami under tension. Soft Matter 13, 8930–8939.

Hwang, D.G., Bartlett, M.D., 2018. Tunable mechanical metamaterials through hybrid kirigami structures. Sci. Rep. 8, 3378.

Isobe, M., Okumura, K., 2016. Initial rigid response and softening transition of highly stretchable kirigami sheet materials. Sci. Rep. 6, 24758.

Jang, N.S., Kim, K.H., Ha, S.H., Jung, S.H., Lee, H.M., Kim, J.M., 2017. Simple approach to high-performance stretchable heaters based on kirigami patterning of conductive paper for wearable thermotherapy applications. ACS Appl. Mater. Interfaces 9, 19612–19621.

Lamoureux, A., Lee, K., Shlian, M., Forrest, S.R., Shtein, M., 2015. Dynamic kirigami structures for integrated solar tracking. Nat. Commun. 6, 8092.

Lu, N., Yang, S., 2015. Mechanics for stretchable sensors. Curr. Opin. Solid State Mater. Sci. 19, 149–159.

Plimpton, S., 1995. Fast parallel algorithms for short-range molecular-dynamics. J. Comput. Phys. 117, 1–19.

Qi, Z., Campbell, D.K., Park, H.S., 2014. Atomistic simulations of tension-induced large deformation and stretchability in graphene kirigami. Phys. Rev. B 90.

Rafsanjani, A., Bertoldi, K., 2017. Buckling-Induced kirigami. Phys. Rev. Lett. 118, 084301.

Shan, S., Kang, S.H., Zhao, Z., Fang, L., Bertoldi, K., 2015. Design of planar isotropic negative Poisson's ratio structures. Extreme Mech. Lett. 4, 96–102.

Shyu, T.C., Damasceno, P.F., Dodd, P.M., Lamoureux, A., Xu, L., Shlian, M., Shtein, M.,

Glotzer, S.C., Kotov, N.A., 2015. A kirigami approach to engineering elasticity in nanocomposites through patterned defects. Nat. Mater. 14, 785–789.
Tang, Y., Lin, G., Han, L., Qiu, S., Yang, S., Yin, J., 2015. Design of hierarchically cut hinges for highly stretchable and reconfigurable metamaterials with enhanced strength. Adv. Mater. 27, 7181–7190.
Tang, Y., Lin, G., Yang, S., Yi, Y.K., Kamien, R.D., Yin, J., 2017. Programmable kiri-kirigami metamaterials. Adv. Mater. 29, 1–9.
Tang, Y., Yin, J., 2017. Design of cut unit geometry in hierarchical kirigami-based auxetic metamaterials for high stretchability and compressibility. Extreme Mech. Lett. 12, 77–85.
Timoshenko, S.P., Goodier, J.N., 1970. Theory of Elasticity, third ed. McGraw-Hill Companies, New York.
Wang, W., Li, C., Rodrigue, H., Yuan, F., Han, M.-.W., Cho, M., Ahn, S.-.H., 2017. Kirigami/origami-based soft deployable reflector for optical beam steering. Adv. Funct. Mater. 27, 1604214.
Widlund, T., Yang, S., Hsu, Y.-.Y., Lu, N., 2014. Stretchability and compliance of free-standing serpentine-shaped ribbons. Int. J. Solids Struct. 51, 4026–4037.
Wu, C., Wang, X., Lin, L., Guo, H., Wang, Z.L., 2016. Paper-Based triboelectric nanogenerators made of stretchable interlocking kirigami patterns. ACS Nano 10, 4652–4659.
Xu, L., Wang, X., Kim, Y., Shyu, T.C., Lyu, J., Kotov, N.A., 2016. Kirigami nanocomposites as wide-angle diffraction gratings. ACS Nano 10, 6156–6162.
Yang, S., Qiao, S., Lu, N., 2016. Elasticity solutions to nonbuckling serpentine ribbons. J. Appl. Mech. 84, 021004.
Yang, Y., Dias, M.A., Holmes, D.P., 2018. Multistable kirigami for tunable architected materials. Phys. Rev. Mater. 2 110601(R).
Zhang, Y., Xu, S., Fu, H., Lee, J., Su, J., Hwang, K.C., Rogers, J.A., Huang, Y., 2013. Buckling in serpentine microstructures and applications in elastomer-supported ultra-stretchable electronics with high areal coverage. Soft Matter 9, 8062–8070.